Development and validation of a potent and specific inhibitor provides evidence for the CLC-2 chloride channel as a potential epilepsy target

Anna K. Koster, Austin L. Reese, Yuri Kuryshev, Xianlan Wen, Adam C. Lu, Keri A. McKiernan, Erin E. Gray, Caiyun Wu, Mark P. Beenhakker, John R. Huguenard, Merritt Maduke, J. Du Bois

Summary

CLC-2 is a voltage-gated chloride channel expressed ubiquitously in mammalian tissue. Studies to define how CLC-2 contributes to normal and pathophysiological brain function have produced controversial results, in part due to the absence of precise pharmacological tools for modulating CLC-2 function. Herein, we describe the development and optimization of a new small-molecule inhibitor of CLC-2, AK-42, that exhibits unprecedented potency and specificity. Computational docking, validated by mutagenesis and kinetic studies, indicates that AK-42 binds to an extracellular vestibule above the channel pore. AK-42 acutely and specifically inhibits CLC-2 currents in CA1 hippocampal pyramidal neurons. Use of AK-42 in an established thalamic-slice model for studying epilepsy suggests a role for CLC-2 in modulating electrical excitability and implicates CLC-2 as a possible anti-epileptic target. These results establish AK-42 as a powerful new tool for investigating CLC-2 physiology in the central nervous system.

Introduction

Although Cl^- is the most abundant anion in the brain, its role in neuronal signaling has been subject to less scrutiny relative to cations, such as Na^+, K^+, and Ca^{2+}. The inattention to Cl^- may be traced back to the pioneering work on neuronal action potentials by Hodgkin and Huxley, who characterized Cl^- as responsible for only minor "leak" currents[1]. While it is now recognized that Cl^- movement is critical for homeostatic functions in the brain, including regulation of cell volume and pH[2-6], the role of Cl^- in excitability remains incompletely understood. The best-studied effects of Cl^- on excitability are at GABAergic synapses, the major inhibitory synapses in the mammalian brain[7,8]. A voltage-gated chloride channel, CLC-2, is also widely expressed in the central nervous system (CNS), but its function remains poorly defined.

The CLC-2 channel belongs to the "CLC" family of Cl^--selective ion channels and transporters, of which there are nine mammalian homologs[9]. CLC-2 is activated by hyperpolarization of the plasma membrane and is expressed in nearly every tissue-type, including brain, heart, intestines, and lungs[10]. Interest in CLC-2 physiology in the CNS was sparked by CLC-2 knockout mouse phenotypes, which display severe deficiencies, including retinal degeneration/blindness and vacuolization of myelin in brain tissue[11-13]. In addition, human patient data suggest a link between CLC-2 malfunction and certain forms of generalized epilepsies[14-21]. Although a causative role for CLC-2 underlying genetic disease remains controversial[22,23], the available research, together with the widespread expression of CLC-2 in the CNS[10,11,24-28], motivate further examination of this channel.

Understanding CLC-2 physiology has proven difficult in the absence of selective and specific chemical reagents for labeling and modulating the activity of this ion channel. Commercially available Cl^--channel inhibitors[29] lack potency, with mid-μM to mM concentrations required to achieve inhibition of Cl^- current[9,30-32]. These molecules also generally lack selectivity against the different types of Cl^- channels, which strictly limits the usefulness of these compounds for cellular and organismal studies. For the CLC channels, the most potent and selective small-molecule inhibitors are those targeting CLC-Ka, one of two CLC homologs expressed in the kidney[33-36]. For CLC-2, the only reported small-molecule (non-peptide) inhibitors require application of high concentrations (~1 mM)[9,10,24,37]. CLC-2 is also inhibited by low μM concentrations of the divalent cations, Cd^{2+} and Zn^{2+} [38,39]; however, these ions are toxic and lack subtype specificity. A peptide toxin, GaTx2, has been reported to selectively inhibit CLC-2 at concentrations of ~20 pM[40]; however, current inhibition saturates at ~50% with the application of GaTx2, thus restricting use of this toxin as a pharmacological probe. The dearth of high-affinity, high-precision tool compounds for investigating CLC-2 physiology inspires the studies described herein.

Screening for new CLC-2 inhibitors

Using the IonWorks™ Barracuda (IWB) automated patch-clamp platform, we performed a focused screen of FDA-approved drug molecules against human CLC-2 stably expressed in Chinese hamster ovary (CHO) cells and identified meclofenamate (MCFA) as a 'hit' compound (**Figure 1**, **Extended Data Figure 1**, **Extended Data Table 1**, **Supplementary Table 1**). MCFA was selected over other 'hits' owing to the ease of synthesis and

modification of the diarylamine core. Examination of other non-steroidal anti-inflammatory drugs (NSAID) within our initial screen (**Extended Data Table 1**) revealed that the interaction of MCFA with CLC-2 does not simply derive from non-specific Coulombic attraction of the anionic carboxylate group to the electropositive ion conduction pore. Most notably, mefenamic acid and diclofenac, which are structurally analogous to MCFA, have negligible inhibitory activity at 30 μM. A small collection of angiotensin (AT1) receptor antagonists called sartans that are anionic at physiological pH due to the presence of a tetrazole, carboxylic acid, or both also failed to inhibit Cl^- currents to any appreciable extent at 30 μM. Other reported small-molecule modulators of CLC channels (BIM1, BIM4, DPC, NFA, and lubiprostone)[34,36,37,41,42] displayed no efficacy against CLC-2 (**Extended Data Table 1)**.

Structure-Activity Relationship (SAR) studies

To enable SAR studies of MCFA, we developed a general synthesis of substituted diarylamines (**Figure 1A**). Using this strategy, we prepared a total of 51 MCFA derivatives. The results from evaluation of the first 37 derivatives tested (**Figure 1B)** guided the design of an additional 14 compounds (**Extended Data Figure 2**).

An initial systematic examination was performed to assess the effects of –Cl and –Me substituents on the western aryl ring of the MCFA scaffold (**Figure 1**, green, orange, and red boxes). Removal of either the C2- or C6-Cl group (AK-3, AK-6) resulted in a ~50% decrease in potency relative to MCFA. By contrast, the potency of AK-4, which lacks the C3-Me group, was unchanged. Other di- and tri-chlorinated analogs, including AK-1, AK-2, AK-5, and AK-7, were ineffective at blocking CLC-2 ($IC_{50} \geq 120$ μM). C2,C6-Substitution with Cl- or Me-groups (AK-4 and AK-15, respectively) proved imperative; introduction of sterically smaller (–F, AK-8) or larger (–Et, AK-21) substituents significantly reduced inhibitor potency. These results suggest that a twisted geometry of the diarylamine scaffold is necessary for inhibition.

The mildly enhanced potency of MCFA over AK-4 (IC_{50} = 14 μM vs. 22 μM) led us to query the effect of replacing the C3-Me group in MCFA with alternative substituents (**Figure 1**, blue box). Initially, a series of four compounds was prepared in which a –OMe, isopropenyl, –Et, or $–CF_3$ group was introduced at C3 (AK-13, AK-14, AK-16, and AK-17, respectively). With the exception of AK-17, these ligands were nearly 2-fold more potent

than MCFA. In a second round of SAR, incorporation of sterically larger groups at C3, which included –OBn, –Ph, and –$OCH_2{}^cHx$ (AK-24, AK-25, and AK-26, respectively), resulted in an additional enhancement in potency. Among these derivatives, AK-24 was identified as the most effective inhibitor of CLC-2 with an IC_{50} of 0.6 μM.

We next evaluated the influence of the MCFA carboxylate group on ligand binding (**Figure 1**, purple). This study included moving the position of the carboxylate from C1' to C5' and C6' on the eastern ring (AK-20, AK-19) and replacing the carboxylate with other charged substituents, including $–OSO_3^–$, $–PO_3^{2–}$, $–PO_2(OEt)^–$, –tetrazolate, and $–CH_2CO_2^–$ (AK-9, AK-34, AK-35, AK-18, and diclofenac, respectively). A neutral analog of MCFA, AK-36, in which the carboxylate group was converted to a primary carboxamide, was also prepared. All eight of these compounds displayed reduced potency relative to MCFA. From these data, the efficacy of carboxamide AK-36 is perhaps most surprising, as this derivative is only ~3-fold less potent than MCFA despite lacking the anionic charge. This result indicates that ligand-protein binding is not purely dictated by charge-charge interactions.

Additional ligand SAR effects were revealed by varying substituent groups on the eastern ring of MCFA with the western ring held fixed (**Figure 1**, magenta and cyan). A methyl scan at positions C4', C5', and C6' (AK-10, AK-11, and AK-12, respectively) showed diminished potency for all three isomers, with the most significant loss resulting from C6' substitution. Collectively, these findings intimate that the eastern ring of MCFA is sequestered in a restricted binding pocket. Given these data, we prepared four isomeric nicotinic acid derivatives (AK-30, AK-31, AK-32, and AK-33), reasoning that introduction of a N-atom in this region of the inhibitor would alter steric size and potentially enable stabilizing hydrogen bonding interactions with the protein. While three of these compounds display substantially reduced potency, the potency of one derivative, AK-33, is improved 7-fold over MCFA (IC_{50} = 2 μM). Given that these isomers should have similar cLogP values and polar surface areas, this finding suggests that the N-atom at the 3' position engages in a specific interaction between AK-33 and CLC-2.

In light of our results with AK-24 and AK-33, we synthesized AK-42, a derivative that combines the C3-OBn substituent on the western ring with the C3'-nicotinic acid on the eastern half (**Figure 2A**). AK-42 is almost *three orders of magnitude* more potent than MCFA (**Figure 2B**). Manual patch-clamp experiments on CHO cells

transiently transfected with rat CLC-2 indicate comparable AK-42 potency to that determined for human CLC-2 using the IWB (**Extended Data Figure 3**, IC_{50} value of 14 nM for rat CLC-2**)**. To our knowledge, AK-42 is the most potent small-molecule inhibitor against any CLC homolog.

AK-42 selectivity, specificity, and binding site

To assess the utility of AK-42 as a tool compound for studies of CLC-2 physiology, we evaluated the selectivity of this ligand for CLC-2 over other protein targets. Electrophysiological recordings of CLC-1, the most closely related homolog to CLC-2 (55% sequence identity), revealed >4 orders of magnitude reduced sensitivity to AK-42 (**Figure 2C**). By comparison, the original 'hit' compound, MCFA exhibits only modest selectivity (<10-fold) between the two homologs (**Extended Data Table 3**).

AK-42 was next tested against a broad panel of channels, receptors, and transporters, using a comprehensive screen developed and conducted by the National Institutes of Health Psychoactive Drug Screening Program (NIH PDSP) to evaluate the specificity of small-molecules against CNS targets[43]. Depending on the identity of the receptor, primary binding assays or functional assays were performed with each compound at 10 μM, a concentration well above the IC_{50} of AK-42 for CLC-2 and at least 4 times higher than the inhibitor concentrations used in our primary cell experiments (*vide infra*). In these assays, no notable off-target protein-binding effects were observed; for the 8 targets exhibiting a response of >50% at 10 μM (**Supplemental Table 2**), secondary assays confirmed that the effects were weak or negligible (**Supplemental Figure 2**).

To gain insight into the molecular basis for the CLC homolog selectivity, we performed a computational docking study and experimentally tested the binding-site predictions. Absent a high-resolution structure of CLC-2, we took advantage of a CLC-2 structural homology model we had developed and refined with 600 μs of molecular dynamics simulations[44]. Based on the kinetics and reversibility of inhibition (**Extended Data Figures 3, 4**), we reasoned that AK-42 is likely binding to the extracellular side of channel pore. Docking of AK-42 to the extracellular side of the CLC-2 model preferentially places this ligand near the outer vestibule of the ion-permeation pathway, in a similar site to that targeted by anionic inhibitors in CLC-Ka[35,36]. Notably, we found that AK-42 does not dock to the cryo-EM structure of CLC-1 (6COY)[45], in line with our functional studies on

selectivity (**Figure 2C**). While the top docking poses in our CLC-2 model vary in the specific interactions predicted, all place AK-42 in the same general binding site. A representative docking pose to the predicted CLC-2 binding site, along with a schematic of the 14 residues observed near AK-42 in all models, is shown in **Figure 3A, B**.

To test the binding-site predictions of this model, we first examined mutations at the two charged residues located within this proposed pocket, K210 and K400, reasoning that at least one of these could contribute to electrostatic stabilization of the anionic inhibitor molecule. Mutations at K210, a highly conserved residue, resulted in significantly diminished sensitivity to AK-42 (**Figure 3C, D**). Notably, the effectiveness of AK-42 is reduced even against the charge-conserved mutant, K210R. Accordingly, the K210 residue may play a critical role in fixing the inhibitor geometry within the binding pocket, as suggested in the binding pose illustrated in **Figure 3B.** By contrast, no change in inhibitor sensitivity is measured against the mutant K400R, as compared to WT. These results confirm that the charge at K400 does not contribute to inhibitor selectivity for CLC-2 over CLC-1, the latter of which bears an arginine at this position. Finally, introduction of proline at Q399, the residue present at the equivalent position in CLC-1, reduces inhibition by AK-42 (**Figure 3D**). Together, these data support our conclusion that AK-42 binds to the predicted extracellular site on CLC-2.

Validation of AK-42 in brain-slice recordings

To validate the utility of AK-42 in neurophysiological studies, we measured CLC-2 currents in CA1 pyramidal cells of acute brain slices using whole-cell patch-clamp electrophysiology. CLC-2 currents were isolated by blocking synaptic transmission and currents mediated by voltage-gated sodium channels and hyperpolarization-activated cyclic nucleotide–gated (HCN) channels (see **Methods**). To evoke CLC-2 currents, cells were stepped from –4 mV, a membrane potential at which CLC-2 channels are closed, to test potentials ranging from –100 to 30 mV. During the 3-second test pulse, CLC-2 current is observed as a slow increase in inward current at the most negative potentials (**Figure 4A**). Relative to other neuronal ion channels, the CLC-2 channel activates slowly (seconds) following hyperpolarization, thereby facilitating current isolation[26,27,46-48]. We measured CLC-2 channel activity both in terms of the final steady-state current, as well as the amount of current change over the

4-second test step (relaxation current). Our lead compound AK-42 attenuated steady-state currents and eliminated relaxation currents in recorded neurons (**Figure 4A–D**) but had no effect on either measurement in neurons recorded from homozygous CLC-2 knockout (*Clcn2*$^{-/-}$) mice, thereby demonstrating target specificity (**Figure 4E–H**; **Extended Data Figure 5A–B**). These initial observations, obtained at 2.5 uM AK-2, were confirmed in experiments using a lower, but still saturating, concentration of 100 nM (**Extended Data Figure 5C–E**). Specificity of the inhibition was further supported by experiments showing 100 nM AK-42 has no effect on firing rate, resting membrane potential, input resistance, or membrane time constant (**Extended Data Figure 5F–I**).

Using the same tissue preparation, the time course for inhibition by AK-42 (100 nM) was measured (**Extended Data Figure 5C**). Steady-state inhibition of CLC-2 current recorded at –80 mV in hippocampal neurons was achieved within 5–10 minutes of compound application to brain slices. AK-42 had no effect on currents recorded at –20 mV, a voltage at which little to no CLC-2 current is expected. The 5–10 minute time course for onset of inhibition is slower than the rates derived from our kinetic assays in CHO cells, but such differences are expected for a compound that must penetrate tissue to reach the intended target. Following steady-state inhibition, we evaluated reversibility by washing out AK-42 (perfusion with buffer solution) over several minutes (**Extended Data Figure 5C**). Substantial recovery of hyperpolarization-induced current (66%) supports our hypothesis that the AK-42 binding site is extracellular, that the compound is not significantly internalized over the course of the experiment, and that this new probe can provide a method for acute, selective, and reversible block of CLC-2 in primary neurons.

AK-42 reveals that CLC-2 activity is seizure-protective

Having established the specificity of AK-42 for CLC-2, and given the potential role of CLC-2 in regulation of excitability and epilepsy[15-21], we examined the effect of AK-42 on neural network excitability in a brain slice model of epilepsy that contains the thalamus, a subcortical structure. CLC-2 is enriched in the dorsal and reticular thalamus[27,49], two thalamic nuclei implicated in producing seizures associated with generalized epilepsies[50-52]. Rhythmic epileptiform oscillations, which can be evoked in acute brain slices containing the two thalamic nuclei, have long served as an important model to better understand mechanisms that regulate network excitability and

mediate anti-epileptic drug actions[53-55]. We therefore evaluated the effects of AK-42 on bicuculline-enhanced thalamic oscillations in acute rat brain slices, a robust model of epileptic activity[56-58]. Seconds-long network oscillations were reliably evoked by electrical stimuli (**Figure 5A**). Oscillations were evoked while delivering control recording solution (ACSF with 0.001% DMSO) to slices for 20 minutes (baseline), followed by solutions containing either 100 nM AK-42 (in 0.001% DMSO) or a vehicle control (0.001% DMSO, **Figure 5B**, **C**); the experimenter was blinded to the condition. Application of the DMSO vehicle did not change the duration of evoked oscillations (**Figure 5D**, P = 0.34, n = 7). In contrast, AK-42 application reduced the oscillation duration by an average 0.81 s (17%) (**Figure 5D**, P = 0.0015, n = 12). These data show that CLC-2 inhibition suppresses epileptiform activity *in vitro* and suggest that CLC-2 inhibitors could be a target for anti-epileptic drug therapies.

Discussion

AK-42 represents the first molecular tool for precisely disentangling the complex effects of CLC-2 in the CNS. The high potency and specificity of AK-42 for its target stands in contrast to all other known Cl^- channel small-molecule modulators and enables acute channel inhibition, thus avoiding the interpretive challenges of genetic knockout or silencing methods. AK-42 was systematically advanced from an initial hit compound, MCFA. With an IC_{50} of 17 ± 1 nM, AK-42 is ~10,000 times more potent against human CLC-2 versus the next closest homolog, CLC-1. In addition to extraordinary selectivity within the CLC family, AK-42 is highly specific for CLC-2 as compared to other CNS channels, receptors, and transporters. Moreover, AK-42 acutely and specifically inhibits CLC-2-mediated current in WT hippocampal CA1 neurons recorded in brain slices, and it is reversible on the timescale of a typical brain-slice experiment. The discovery of AK-42 represents a breakthrough in CLC channel pharmacology and will enable systematic investigations of CLC-2 function.

The molecular physiology of CLC-2 remains poorly understood. Data from mouse genetic knockout studies suggest a critical role for CLC-2 in ion homeostasis and electrical excitability in the CNS, but discrete mechanisms that underlie CLC-2 activity have been difficult to elucidate in the absence of specific and potent chemical modulators of CLC-2. Two lines of experiments suggest a role for the CLC-2 channel in maintaining strong inhibitory responses at GABAergic synapses[48,59]. Activation of the $GABA_A$ receptor opens a chloride-conductive

pore within the receptor that permits the rapid influx of negatively charged Cl^- ions into cells, causing a voltage hyperpolarization that represents the primary mode of synaptic inhibition in the CNS. To ensure Cl^- influx, low intracellular concentrations of the ion must be maintained; the accumulation of intracellular Cl^- following rapid and successive activation of $GABA_A$ receptors can lead to cellular depolarization, a result of Cl^- efflux[59-62]. The properties of CLC-2—chiefly, Cl^- extrusion following hyperpolarization—are thus hypothesized to provide an important means for maintaining low intracellular Cl^- concentration following synaptic inhibition[26,48,59]. Alternatively, it has been argued that CLC-2 regulates neuronal excitability, not by maintaining low intracellular Cl^- concentrations through Cl^- efflux, but rather by mediating Cl^- *influx* under physiological conditions[63].

Both of the above proposals lead to the same hypothesis: genetic loss-of-function should result in excessive neural circuit activity and contribute to the generation of seizures. Consistent with this hypothesis, an early study reported human CLC-2 mutations as contributing to several major genetic generalized epilepsy (GGE) subtypes[14]. This original study was retracted, however, and since this time, the role of CLC-2 in regulating seizures has been controversial[16,17,20-22]. Given that connections between CLC-2 mutations and epilepsies are rare in the GGE population[15,18,19], it is likely that such mutations are susceptibility factors, a conclusion that generally underscores the emerging hypothesis that the common, genetically-acquired epilepsy subtypes are complex, polygenic disorders that do not arise from single mutations[64-67].

In our experiments using a well-established thalamic model of epilepsy[56-58], we inhibited CLC-2 pharmacologically and acutely, eliminating complications in experimental interpretation that may occur as a result of developmental changes in modified genetic backgrounds. Our finding that inhibition of CLC-2 causes a *downregulation* of network activity is the opposite of expected based on a causal link between CLC-2 loss-of-function and epilepsy; rather, our data implicate CLC-2 as a putative target for anti-epileptics. Despite the unexpected nature of this finding, there are many potential mechanisms that might result in the anti-epileptic effects of CLC-2 inhibition, including intrinsic, e.g., alteration in neuronal excitability[63], extrinsic (non-neuronal, e.g., astrocytic[68]), or synaptic[48], among others. Our discovery of AK-42, a potent and specific CLC-2 inhibitor, will enable future studies to determine the mechanism by which CLC-2 regulates excitability.

Supplementary Information All results from the ENZO library screen are available in **Supplemental Table 1**. All specificity data from PDSP are available in **Supplemental Table 2**. Detailed chemical synthesis protocols and characterization data for all inhibitors and intermediates are provided in **Chemistry Supplemental Information**.

Acknowledgements Receptor binding profiles and agonist/antagonist functional data were generously provided by the National Institute of Mental Health's Psychoactive Drug Screening Program, Contract #HHSN-271-2018-00023-C (NIMH PDSP). The NIMH PDSP is directed by Bryan L. Roth MD, PhD at the University of North Carolina at Chapel Hill and Project Officer Jamie Driscoll at NIMH, Bethesda, MD, USA. *Clcn2*$^{-/-}$ mice were generously provided by J. Melvin (University of Rochester). The CLC-2 construct used for manual patch-clamp recordings was kindly provided by M. Pusch (Istituto di Biofisica, Genova, Italy). This work was supported by a Stanford Bio-X Seed grant (to J.D.B and M.M.). A.K.K. and K.A.M. were supported by the Stanford Center for Molecular Analysis and Design (CMAD). A.K.K. was also supported by a Stanford Interdisciplinary Graduate Fellowship (SIGF) through the Stanford ChEM-H Institute.

Author Contributions A.K.K., J.D.B., and M.M. designed the inhibitors. A.K.K. designed and executed the synthetic route for all inhibitors and chemical intermediates. E.E.G. synthesized a subset of molecules for the final round of SAR. Y.K. performed all IWB-based screening assays and kinetic studies. C.W. developed the original CLC-2 assay protocol for the IWB platform. K.A.M developed the computational CLC-2 homology models. K.A.M. and A.K.K. performed computational docking studies. A.K.K. and X.W. developed the CHO cell manual patch-clamp recording protocols and performed site-directed mutagenesis. X.W. collected and analyzed all CHO cell manual patch-clamp data presented in this manuscript. A.L.R. and J.R.H. designed and executed mouse slice recording experiments and analyzed the data. M.P.B. and A.C.L. designed and executed thalamic slice recording experiments and interpreted the data. A.K.K., J.D.B., and M.M. wrote the manuscript with input from all authors.

Corresponding Authors

Correspondence to J. Du Bois or Merritt Maduke or John R. Huguenard

Author Affiliation

Department of Chemistry, Stanford University, Stanford, CA, USA

Anna K. Koster, Erin E. Gray, Keri A. McKiernan, J. Du Bois

Department of Molecular & Cellular Physiology, Stanford University School of Medicine, Stanford, CA, USA

Anna K. Koster, Xianlan Wen, Merritt Maduke

Department of Neurology & Neurological Sciences, Stanford University School of Medicine, Stanford, CA, USA

Austin L. Reese, John R. Huguenard

Charles River Laboratories, Cleveland, OH, USA

Yuri Kuryshev, Caiyun Wu

Department of Pharmacology, University of Virginia School of Medicine, Charlottesville, VA, USA

Mark P. Beenhakker, Adam C. Lu

Methods

IonWorks™ Barracuda (IWB) electrophysiology recording conditions

Data acquisition and analyses were performed using the IonWorks™ Barracuda systems (Molecular Devices Corporation, Union City, CA, operation software version 2.5.3.359) in the Population Patch Clamp™ (PPC) Mode. Test article (TA) and positive control concentrations were prepared fresh daily by diluting stock solutions into an extracellular buffer solution, and the TA formulations were loaded in a 384-well compound plate. Currents were recorded from groups of 64 cells. HEPES-buffered intracellular solution (in mM: 50 CsCl, 90 CsF, 5 $MgCl_2$, 5 EGTA, 10 HEPES, pH = 7.2 adjusted with CsOH) for whole-cell recordings was loaded into the intracellular

compartment of the PPC planar electrode. Extracellular buffer (HB-PS; in mM: 137 NaCl, 4 KCl, 3.8 $CaCl_2$, 1 $MgCl_2$, 10 HEPES, 10 Glucose, pH = 7.4 adjusted with NaOH) was loaded into PPC planar electrode plate wells (11 µL per well). The cell suspension was pipetted into the wells of the PPC planar electrode (9 µL per well). After establishment of a whole-cell configuration (the perforated patch; 12 µM escin, 7 min), membrane currents were recorded using patch-clamp amplifier in the IonWorks™ Barracuda system. The current recordings were performed one time before TA application to the cells (baseline) and one time after application of TA or reference compound. Seal resistance prior to compound application was ≥ 200 MΩ. Reference compound concentrations were applied to naïve cells (n = 4, where n = replicates/concentration). Each application consisted of a 20 µL addition of a 2 × concentrated test article solution to the total 40-µL final volume of the extracellular well of the PPC electrode. The addition was followed by a single mixing of the PPC well content. Duration of exposure to each compound concentration was 5 minutes.

Prior to initial screening, we validated our assay by using Cd^{2+} and NPPB as positive controls for CLC-2 inhibition. Eight dose-response curves were generated in each experiment on two different days (n = 3–4 per concentration). All Z' values (a standard metric for evaluating assay quality) exceeded 0.5, indicating acceptable assay variability[69]. The Z' factor was calculated as: $Z' = 1 - (3 \times SD_{VC} + 3 \times SD_{PC})/ABS\ (Mean_{VC} - Mean_{PC})$, where $Mean_{VC}$ and SD_{VC} are the mean and standard deviation values for a vehicle control, and $Mean_{PC}$ and SD_{PC} are the mean and standard deviation values for a positive control (300 µM NPPB or 1 mM Cd^{2+}). Initial screening for hit compounds was performed using the ENZO Life Sciences SCREEN-WELL® FDA-approved drug library, v. 2.0 (Product # BML-2843-0100). All compounds in this library are reported in **Supplemental Table 1**. Vehicle controls of 0.3 or 1.0% DMSO (without compound) in recording solution were applied in replicate as additional controls in each experiment.

Cell line generation

All CLC-2 recordings using the IWB platform were performed using a stably expressing Chinese hamster ovary (CHO) cell line. CHO cells were transfected with human CLC-2 cDNAs (*CLCN2*, GenBank Acc # NM_004366.3). Stable transfectants were selected by expression with the antibiotic-resistance gene (Geneticin/G418) incorporated into the expression plasmid (pcDNA3.1(+)). Selection pressure was maintained by including selection antibiotics in the culture medium. Cells were cultured in Ham's F-12 media (Life Technologies, Grand Island, NY) supplemented with 10% fetal bovine serum (HyCloneTM Fetal Bovine Serum, U.S.), 100 U/mL penicillin G sodium, 100 µg/mL streptomycin sulfate, and 500 µg/mL G418. Before testing, cells in culture dishes were washed twice with Hank's Balanced Salt Solution (HBSS, Life Technologies, Grand Island, NY), treated with Accutase™ (Innovative Cell Technologies, San Diego, CA) solution for 20 min at room temperature, and re-suspended in HBSS (4–6 × 10^6 cells in 10 mL). Immediately before use, the cells were washed twice in HBSS to remove the Accutase™ and re-suspended in 5 mL of HBSS. CLC-1 recordings were performed using a stably expressing CHO cell that was generated according to the same methods described for CLC-2.

IWB voltage protocol and data analysis

From a holding potential of –30 mV, CLC-2 currents were elicited by applying 2-second test pulses from –120 to +20 mV in 20-mV increments. Following each test pulse, a 500-ms tail pulse to 0 mV was applied. We required initial currents at the 0-mV tail pulse to be ≥ 0.2 nA to be included in analysis. All IC_{50} data reported in the manuscript are given according to measurements at the peak inward current at –120 mV, the point where the maximum number of CLC-2 channels are open. The decrease in current amplitude after compound (TA) application was used to calculate the percent block relative to the positive control, according to the equation: % Inhibition = $(1 - I_{TA} / I_{Baseline}) \times 100\%$, where $I_{Baseline}$ and I_{TA} are the currents measured before and after addition of compound, respectively. The data were then corrected for run-down according to the equation: %Block' = 100% – [(%Block–%PC) × (100% / (%VC–%PC))], where %VC and %PC are the mean values of the current inhibition with the vehicle control and the highest concentration of a reference compound (300 µM Cd^{2+}). The

inhibition curves were fit to the equation: % inhibition = 100 / [1 + ([IC_{50}] / [TA])^n], where [TA] is the concentration of test article, IC_{50} is the concentration of TA producing half-maximal inhibition, n is the Hill coefficient, and % inhibition is the percentage of current inhibited at each concentration of a TA. Nonlinear least squares fits were solved with the XLfit add-in for Excel (Microsoft, Redmond, WA) (initial screening data) or using the Sigmaplot 13.0 (Systat Software, San Jose, CA) regression analysis (final analyses).

For the kinetics experiments (**Extended Data Figure 4**), current was elicited with a 2000-ms voltage step to potential –120 mV followed by 500-ms voltage step to potential 0 mV; the holding potential was –30 mV. The test pulses were repeated with frequency 0.1 Hz. Six stimulations were applied before application of test articles (1-min baseline), and thirty stimulations were performed after application of test articles (5 min). Current amplitudes were measured as the peak inward current at test potential –120 mV and the maximal outward current at test potential 0 mV.

The vehicle control data (0.3% DMSO; n = 32) were averaged for each time point. All data were normalized to the time-matching averaged vehicle control. Then data were normalized to the baseline current recorded before application of test articles.

Cell culture & recording protocols (manual patch-clamp)

CHO K1 cells (ATCC® CCL-61TM) were cultured at 37 °C in F12K media (ATCC, Catalog No. 30-2004) supplemented with 10% fetal bovine serum (GIBCO) and 1% penicillin/streptomycin (GIBCO). At 70–90% confluency, cells were transfected with full-length rat CLC-2 cDNA (449 ng), using Lipofectamine® LTX, opti-MEM®, and PLUS™ reagent (Invitrogen). The rat CLC-2 gene was contained in a custom plasmid vector called pFROG (ampicillin resistance), provided by Prof. Michael Pusch (Istituto di Biofisica, CNR, Genova, Italy). Co-transfection with GFP (177 ng, 2.5:1 CLC-2/GFP) was used to estimate transfection efficiency. Cells were transfected 18 hours prior to recording. Borosilicate glass micropipettes (Sutter Instruments, Novato, CA) were pulled and fire-polished to a tip diameter with a resistance of 1.5–3.0 MΩ. For whole-cell patch clamp recordings, the internal solution was composed of 148 mM CsCl, 2 mM $CaCl_2$, 10 mM HEPES, and 100 mM D-mannitol (adjusted to pH 7.4 with 2 M aqueous CsOH). The external solution was composed of 146 mM CsCl, 5 mM

EGTA, 10 mM HEPES, 5 mM NaF, and 60 mM D-mannitol (adjusted to pH 7.4 with 2 M aqueous CsOH). If necessary, the osmolarity was adjusted with D-mannitol such that it was slightly higher outside than inside in order to prevent cell swelling, which can make it difficult to establish a high-resistance seal. CLC-2 currents were measured in whole-cell patch-clamp mode, using an Axopatch-200B amplifier (Axon Instruments, Union City, CA), an InstruTECH ITC-16 interface (HEKA Instruments, Holliston, MA), and a Mac mini computer (Apple, Cupertino, CA). Igor Pro (WaveMetrics, Portland, OR) software was used for stimulation and data collection. The data were sampled at 5 kHz and filtered at 1 kHz. From a holding potential of 0 mV, currents were elicited with 250-ms voltage steps of –100 to +20 mV in 10-mV increments, followed by a 100-ms tail pulse to +80 mV (**Figure 3C**). All experiments were carried out at room temperature (22–25 °C). For recording, currents were measured before application of inhibitor ("initial"), after application of inhibitor ("inhibited"), and after washout of inhibitor ("washout"). For fitting dose-response curves (**Extended Data Figure 3**), we excluded experiments in which there was poor reversibility of inhibition. Poor reversibility was defined as when reversal current differed by >20% from initial current and/or inhibition calculated using washout current differed by >10% from inhibition calculated using initial current. An IC_{50} value and a Hill coefficient (n) were obtained with Sigmaplot 13.0 (Systat Software, San Jose, CA) by fitting dose-response curves to the following equation: $I (\%) = 1 / [1 + (IC_{50} / [TA])^n]$, in which I (%) is the percentage current inhibition ($I (\%) = [1 - I_{inhibited} / I_{initial}] \times 100$) at the –100 mV test potential, and [TA] represents various concentrations of inhibitor. Results were each expressed as a mean ± SEM. Analysis of variance (ANOVA) was used for statistical analysis.

Mutagenesis strategy

CLC-2 mutants were generated by site-directed mutagenesis using a QuickChange XL Site-Directed Mutagenesis Kit (Agilent Technologies, Cedar Creek, TX). The following table lists primers used to generate expression vectors in this study.

Vector	Primer	Sequence
pFROG-CLC-2 K400R	Forward	GACAGCTCTCACAG**CGG**GAGACCC
	Reverse	GGGTCTC**CCG**CTGTGAGAGCTGTCC
pFROG-CLC-2	Forward	CAGCTCTCA**CCC**AAAGAGACCCTGGTCAC

Q399P	Reverse	GGTCTCTTT**GGG**TGAGAGCTGTCCGGCC
pFROG-CLC-2 K210M	Forward	CCTTGGA**ATG**GAGGGACCCTTTGTGCAC
	Reverse	GTCCCTC**CAT**TCCAAGGGGCATCCC
pFROG-CLC-2 K210R	Forward	CCTTGGA**AGA**GAGGGACCCTTTGTGCAC
	Reverse	GTCCCTC**TCT**TCCAAGGGGCATCCC

PDSP screening results

AK-42 was screened against a panel of receptors, transporters, and ion channels to examine specificity for CLC-2 in CNS tissue. A comprehensive primary binding assay screen was performed through the NIH Psychoactive Drug Screening Program (PDSP) at UNC-Chapel Hill. Secondary or functional assays were performed for compounds showing >50% activity in the primary assay. All results are shown in **Supplemental Table 2**.

CLC-2 KO mice

Heterozygous CLC-2 KO mice (*Clcn*2$^{+/-}$)[13] were bred and litters genotyped to identify littermate *Clcn*2$^{-/-}$ and *Clcn*2$^{+/+}$ mice, which were paired in each experiment. On any experimental day, brain slices from a pair of young mice (P30–P45) were prepared, and then slices separated by group with the identity blinded to the investigator.

Electrophysiological recordings in acute hippocampal slices

250 µM thick coronal slices were prepared from 30–35 day old WT C57/B6J or KO (*Clcn*2$^{-/-}$) mice as described previously[58]. After recovery for 1 hour, slices were transferred to a recording chamber at 23.5 °C containing oxygenated ACSF (in mM): 2.5 KCl, 10 glucose, 10 CsCl, 116 NaCl, 1.25 sodium phosphate hydrate, 1.0 $MgSO_4$, 2.0 $CaCl_2$, 26 $NaHCO_3$. Whole-cell voltage-clamp recordings were made under constant perfusion at room temperature from CA1 hippocampal pyramidal cells under conditions that isolate and promote stable recordings of hyperpolarization-activated CLC-2 currents. These include Cs^+ as the main internal monovalent cation to block K^+ currents, high internal [Cl^-] to make E_{Cl} = 0 mV and facilitate recordings at a physiological membrane potential of –80 mV, 10 mM external Cs^+ to block HCN channels, and 50 µM picrotoxin/1.5 mM kynurenic acid to block synaptic responses. Internal solution for voltage-clamp contained the following (in mM): 10 HEPES, 130 CsCl, 10 EGTA, 3 MgATP, 0.3 Na_2GTP hydrate, 5 QX-314. For long recordings in **Extended**

Data Figure 5, internal solution was modified to include an ATP regenerating system and was comprised of (in mM): 10 HEPES, 125 CsCl, 10 EGTA, 4 MgATP, 0.3 Na_2GTP, 5 QX-314, 15 phosphocreatine disodium hydrate, 50 U/mL creatine phosphokinase. Internal solution for current clamp included (in mM): 105 K-gluconate, 10 HEPES, 10 NaCl, 20 KCl, 0.6 EGTA, 5 MgATP, 0.3 Na_2GTP. ACSF for current clamp omitted picrotoxin and cesium. Recordings were performed using an Axon Instruments Multiclamp 700A amplifier and Digidata 1550B digitizer (Molecular Devices, San Jose, CA). 10 KHz bessel filtering was applied during the recording.

After achieving whole-cell configuration, cells were allowed to stabilize for 2 minutes before beginning each recording. Recordings in **Extended Data Figure 5** were obtained 2-per-slice: one before AK-42 was added and one after washing the slice for 10 minutes with AK-42. Cell membrane parameters were monitored before and after each voltage-clamp protocol to ensure the stability of each recording. Recordings were excluded if the series resistance was greater than 20 MΩ or changed by more than 25%, or if the holding current at –60 mV exceeded –200 pA. Recordings in **Figure 4** were obtained 1 per slice in ACSF containing either 2.5 μM AK-42 or no inhibitor. Access resistance was measured every 4 minutes. Voltage step protocols were 2 seconds at –4 mV followed by a 3-second step at the test voltage ranging between –100 mV and +20 mV in 10 mV increments before stepping back to –4 mV for 0.5 seconds. Continuous monitoring of whole-cell currents in **Extended Data Figure 5C–E** used a modified voltage protocol utilizing a 4-second conditioning step at –4 mV and a 4-second test step to either –20 or –80 mV. Protocols were run every 30 seconds along with a membrane test.

Data were measured using Clampfit 10.6 (Molecular Devices, San Jose, CA). Steady-state currents were measured as the RMS current in the last 200 ms of the test voltage step. Current relaxation was measured to be the RMS current between 200 and 400 ms into the test voltage step minus the steady-state current. Two-way repeated measures ANOVA was run in GraphPad Prism 6.01 (GraphPad Software, San Diego, CA) to compare treatment groups.

Electrophysiological recordings in acute thalamic slices

400 μm-thick horizontal slices were collected from P11-15 rats. After anesthetization, animals were transcardially perfused with ice-cold protective recovery solution[70] containing (in mM): 92 NMDG, 26 $NaHCO_3$,

25 glucose, 20 HEPES, 10 $MgSO_4$, 5 Na-ascorbate, 3 Na-pyruvate, 2.5 KCl, 2 thiourea, 1.2 NaH_2PO_4, 0.5 $CaCl_2$, titrated to a pH of 7.3–7.4 with HCl. Following extraction, the brain was sliced in ice-cold protective recovery solution, and slices were then incubated at 37 °C for 12 minutes in recovery solution. After incubation, slices were maintained at room temperature ACSF equilibrated with 95% O_2/5% CO_2 and containing (in mM): 126 NaCl, 26 $NaHCO_3$, 10 glucose, 2.5 KCl, 2 $CaCl_2$, 1.25 NaH_2PO_4, 1 $MgSO_4$. Slices were recorded in an interface chamber (BSC1 chamber, AutoMate Scientific, Berkeley, CA) continuously perfused with oxygenated, 34 °C ACSF (2 mL/min). Epileptiform activity was promoted by the addition of 10 μM bicuculline methiode[58] and evoked with a single 500 μs, 10 V electrical stimulus delivered to the reticular thalamus through a pair of 50–100 kΩ bipolar tungsten electrodes (FHC, Bowdoinham, ME). Extracellular multiunit activity was recorded with a single 50–100 kΩ tungsten electrode (FHC) placed within the ventrobasal complex. Signals were recorded with HZP/P511 AC amplifiers (Astromed/Grass Instruments, West Warwick, RI), and then digitized with a Digidata 1440A (Molecular Devices, San Jose, CA). Signals were acquired with pClamp software (Molecular Devices) and filtered at 100–3000 Hz. Custom Matlab (Natick, MA) scripts were used to detect and analyze multiunit activity. After bandpass-filtering the signal at 100–1000 Hz, spikes were detected by checking whether each point with maximum slope, occurring more than 25 ms after stimulation start (to account for the stimulus artifact), crosses a sweep-dependent slope threshold, using a slice-dependent signal-to-noise ratio of 2–3.5. Detected spikes were then grouped into 10-ms bins, from which bursts were detected by setting a minimum burst length of 20 ms and a minimum spike rate within a burst of 100 Hz. The evoked oscillation from each sweep was then defined by the maximum contiguous stretch of bursts starting from stimulation start, with inter-burst intervals no greater than 2000 ms.

Computational Docking

Initial docking studies involved preparation of the receptor and ligand using the dock prep tool in the UCSF Chimera package[71]. The receptor surface and ligand were parameterized using the AMBER parm99 force field[72]. A spacing of 0.3 Å was used for the receptor grid. Initial grids included the entire extracellular surface of the protein. Once prepared, docking calculations were performed using Dock6[73]. These calculations employed flexible docking and yielded 1000 ligand orientations. From this data set, the highest scoring conformations were analyzed. The results revealed clustering of ligands in a single extracellular pocket above the ion permeation pathway. Following identification of a general binding site, additional docking poses were generated for the most potent lead compounds, using the Schrödinger Maestro software suite (Version 2019-2, Schrödinger, LLC, New York, NY, 2019). Prior to docking, ligands were optimized using the OPLS3e[74] force field in LigPrep (Schrödinger, LLC, 2019). Possible ligand tautomers and protonation states at pH 7.0 ± 2.0 were sampled using Epik[75] (Schrödinger, LLC, 2019). Ligands were docked to grids centered on the general binding site (residue K210) for each of the conformational states developed from the CLC-2 homology model described in McKiernan, et al. [44], as well as CLC-2 homology models generated from the 5TQQ and 5TR1 cryo-EM structures of bovine CLC-K[45]. Alignment of the CLC-2 sequence with these structures for generation of the homology models was accomplished with the UCSF Chimera sequence alignment tool[71]. The CLC-2 sequence was then mapped onto the template structure, using the Modeller package[76]. Unresolved regions of the template structure were also refined using Modeller. Docking to the CLC-1 cryo-EM structure (6COY)[77] was performed using a grid centered on the equivalent lysine residue for this homolog (K231). Docking grids were generated using the default Maestro settings for receptor rigidity (Van der Waals radius scaling factor of 1.0 with a partial charge cutoff of 0.25). Prepared ligands were docked to these grids using the default settings for Schrödinger Glide[78] (Schrödinger, LLC, 2019, Van der Waals radius scaling factor of 0.80 with a partial charge cutoff of 0.15). Standard precision (SP) docking was performed with flexible ligand sampling (sampling of nitrogen inversion and ring conformations), and post-docking minimization was performed to generate a maximum of 10 poses per ligand. A representative docking pose is illustrated in **Figure 3**.

Chemical synthesis: General

Reagents were obtained commercially unless otherwise noted. Meclofenamate sodium, *N*-phenylanthranilic acid, and lubiprostone were purchased commercially from Sigma-Aldrich. Diclofenac sodium, indomethacin, and niflumic acid were purchased from Santa Cruz Biotechnology. Salsalate was purchased from ACROS Organics. Aceclofenac was purchased from AK Scientific. Organic solutions were concentrated under reduced pressure (~20 Torr) by rotary evaporation. Air- and moisture-sensitive liquids and solutions were transferred via syringe or stainless steel cannula. Chromatographic purification of final carboxylates, phosphonates, and sulfates was accomplished using high performance liquid chromatography on a C18 column (Alltima C18, 10 μM, 22 × 250 mm or SiliaChrom AQ C18, 5 μM, 10 × 250 mm). Thin layer chromatography was performed on EM Science silica gel 60 F254 plates (250 mm). Visualization of the developed chromatogram was accomplished by fluorescence quenching and by staining with aqueous potassium permanganate or aqueous ceric ammonium molybdate (CAM) solution.

Nuclear magnetic resonance (NMR) spectra were acquired on a Varian Inova spectrometer operating at 300, 400, 500, or 600 MHz for ^{1}H. Spectra are referenced internally according to residual solvent signals. Data for ^{1}H NMR are recorded as follows: chemical shift (δ, ppm), multiplicity (s, singlet; d, doublet; t, triplet; q, quartet; quintet; m, multiplet; br, broad), coupling constant (Hz), integration. Compound concentrations were determined by quantitative NMR, using *N,N*-dimethylformamide as an internal standard in DMSO-d_6. Infrared spectra were recorded as thin films using NaCl plates on a Thermo-Nicolet 300 FT-IR spectrometer and are reported in frequency of absorption. Low-resolution mass spectra were obtained from the Vincent Coates Foundation Mass Spectrometry Laboratory and the Stanford ChEM-H facility, using a Shimadzu 20-20 ESI mass spectrometer and a Phenomenex Synergi 4 μm Hydro-RP 80 Å reversed phase column (30 × 2 mm column, gradient flow 0:1→1:0 MeCN/H_2O with 0.1% formic acid over 4 min). Microwave reactions were performed in a Biotage Initiator microwave reactor.

Inhibitor stock solution preparation and quantification

Meclofenamic acid (MCFA) derivatives were quantified by ^{1}H NMR spectroscopy using distilled *N,N*-dimethylformamide (DMF) as an internal standard. Use of DMF as the internal standard allows for recovery of pure material following lyophilization. Each MCFA derivative was weighed into an Eppendorf tube, using a calibrated analytical balance (Mettler Toledo, Model XS105), and dissolved into DMSO-d_6 to a final concentration of 30–100 mM. To ensure complete dissolution, the sealed Eppendorf tube was inverted at least 5 times and then sonicated for ~60 seconds. Using a calibrated analytical balance, DMF (22 mg) was weighed into a scintillation vial, 3.0 mL DMSO-d_6 (stored in a desiccator jar and preferably newly opened to minimize water contamination in the solvent) was added to the vial via a p1000 micropipette, and the solution thoroughly mixed by inverting the capped vial at least 10 times (note: to prevent cross-contamination between samples and for convenience, disposable micropipette tips may be used without affecting the accuracy of the measurements). To ensure robustness of the quantification protocol, the 100 mM DMF stock solution was independently quantified in triplicate against stock solutions with known concentrations of fumaronitrile dissolved in DMSO-d_6. Fumaronitrile produces a sharp singlet that integrates to 2H at 7.03 ppm in DMSO-d_6 (DMSO solvent residual peak referenced to 2.50 ppm) and may be integrated against either of the DMF methyl signals that appear at 2.73 ppm (3H) and 2.89 (3H) ppm. The average of these three NMR measurements was used for calculation of the final DMF internal standard concentration. All measurements were performed at room temperature. Stock solutions were stored frozen and left at ambient temperature for several hours to thaw and vortexed prior to quantification. A relaxation delay time (d1) of 20 s and an acquisition time (at) of 10 s were used during spectral acquisition. The number of scans was typically set to 32 unless a particular compound concentration was low (< 10 mM) such that more scans were required to improve signal/noise. The concentration of each MCFA derivative was determined by comparison with signal integrations for the MCFA derivative and the DMF internal standard.

FIGURE 1

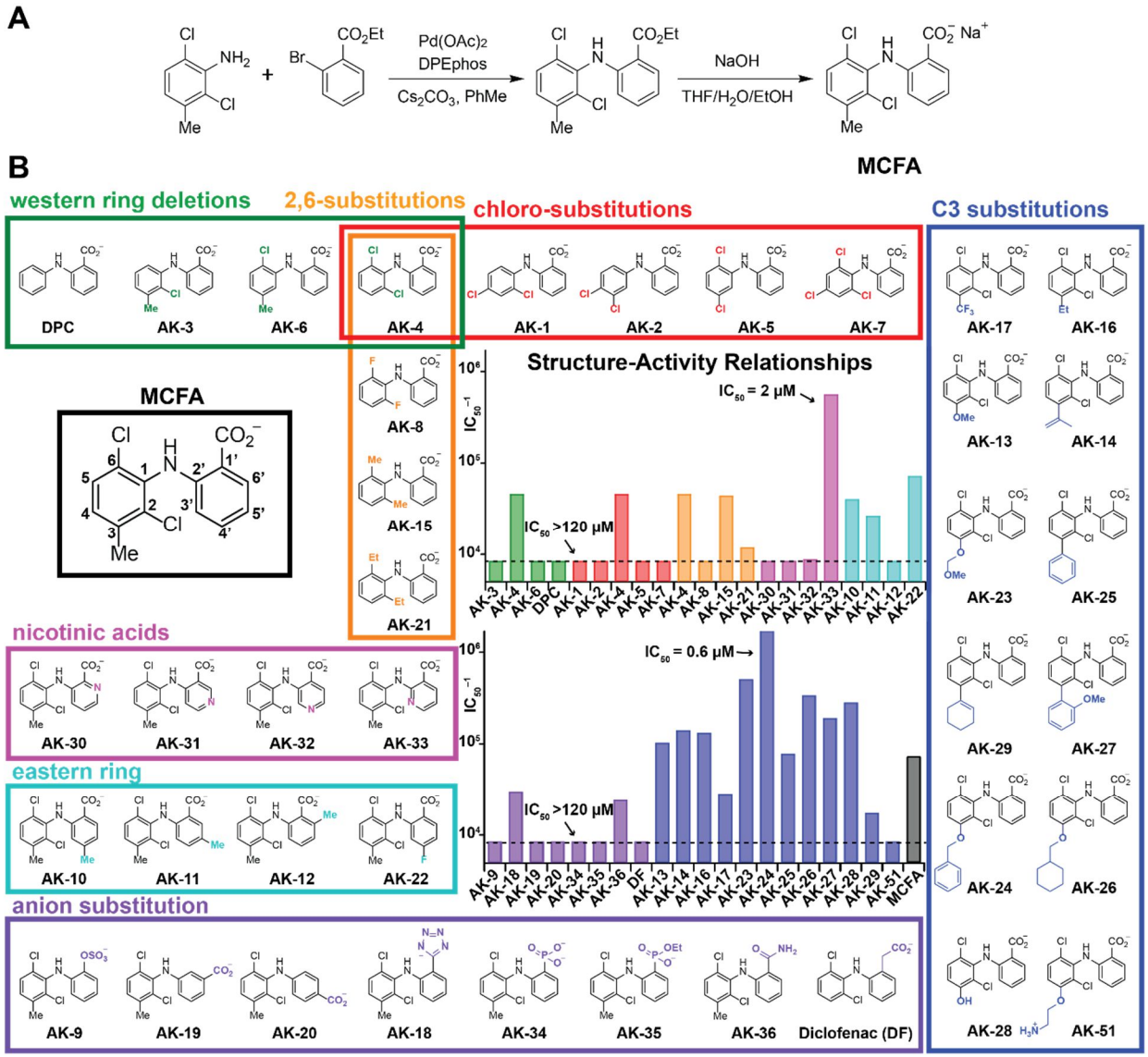

Figure 1. Structure-activity relationship studies to develop a selective CLC-2 inhibitor based on the MCFA 'hit' compound. (**A**) General synthetic route for the preparation of MCFA and analogs. (**B**) SAR of MCFA derivatives. The structure of MCFA is shown left (black box) with carbon numbers of the eastern and western rings labeled. The bar graphs show the inverse IC_{50} for each compound against CLC-2, estimated from inhibition at four concentrations (n = 3–4 each concentration). Compounds are grouped by substitution position, as indicated by bar colors that match the box outlines around each group of structures. Compounds that inhibited weakly at the highest concentration tested (usually 120 μM) are indicated with the dotted line (IC_{50} > 120 μM). Results are tabulated in **Extended Data Table 2**.

EXTENDED DATA FIGURE 1

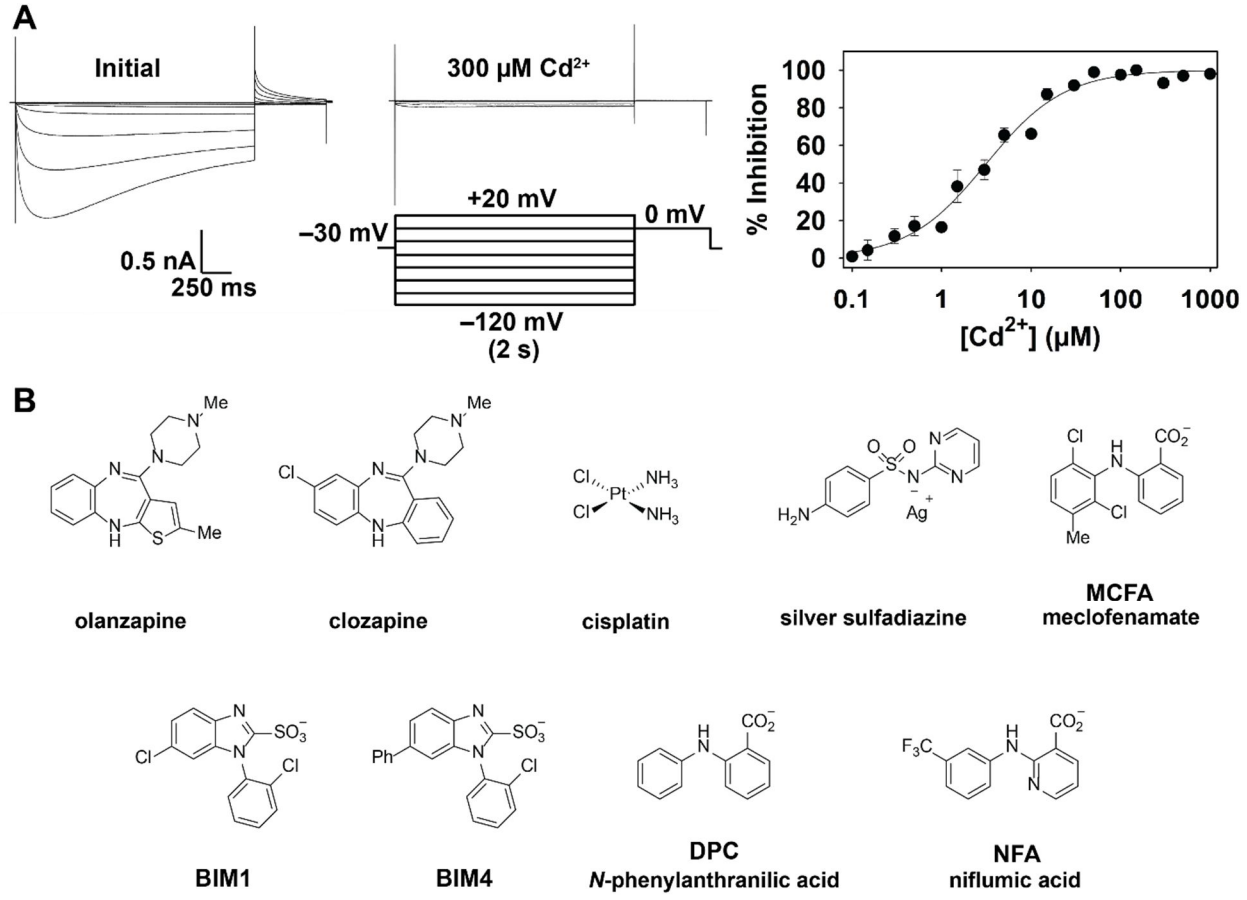

Extended Data Figure 1. CLC-2 assay on the IWB and identification of 'hit' compounds. (**A**) Assay development. *Left:* Representative hCLC-2 currents on IWB measured before (left) or after (right) treatment with positive control Cd^{2+} in response to the voltage protocol shown. The current decay at negative voltages, which is not seen in manual patch-clamp (**Figure 3C** and references[39,79,80] or in a different automated patch-clamp platform (PatchXpress, unpublished data), is likely due to the differences in the intracellular solution, which in this case includes a mixture of Cl^- and F^-. *Right:* Summary data for inhibition of CLC-2 by Cd^{2+} (± SEM, n = 4–32; IC_{50} = 3.1 ± 0.3 μM). Inhibition was calculated using the maximum current at –120 mV in the presence or absence of Cd^{2+}. Assay-validation studies showed a Z-factor of 0.83 and 0.73 on separate days. (**B**) Structures of representative compounds. *Top:* Structures of top five 'hit' compounds identified in the IWB screen of 772 FDA-approved compounds (ENZO Life Sciences). *Bottom:* Representative structures of compounds known to inhibit other CLC channels[36,81] but found to be ineffective inhibitors of CLC-2 in our screen. DPC and NFA, like the 'hit' compound MCFA, are NSAIDs.

EXTENDED DATA TABLE 1

Summary inhibition data for initial 'hit' compounds (>20% inhibition of CLC-2 at –120 mV) and for selected NSAIDs and AT_1 antagonists sampled from the ENZO library. Percent inhibition of CLC-2 current by 30 µM compound at –120 mV is shown for each of two cells. Results from the complete screen (including those shown here) are available in **Supplemental Table 1**. Approximate IC_{50} values of the most potent hit compounds and other selected compounds are shown in the lower right-hand portion of the table. Values were estimated from inhibition measured at 4 concentrations of compound (1, 3, 10, 30 µM, n = 3–4 per concentration) using the IWB platform. For compounds that exhibit little or no inhibition of CLC-2, the IC_{50} is listed as > the highest concentration of compound tested, and the amount of inhibition observed at this concentration is shown in parentheses.

Entry	Compound	% (cell 1)	% (cell 2)
49	Riluzole	20	24
67	Amoxapine	25	26
80	Olmesartan	13	12
82	Olanzapine	56	54
91	Candesartan	12	13
94	Escitalopram	23	25
95	Eprosartan	10	9
127	Clozapine	62	60
136	Indomethacin	–6	10
137	Naproxen	11	15
138	Ibuprofen	9	6
144	Piroxicam	22	19
147	Ketoprofen	2	14
148	Meloxicam	21	23
165	Sulindac	10	11
168	Zafirlukast	27	30
182	Clindamycin Palmitate	20	21
210	Aspirin	16	5
240	Citalopram	19	22
244	Clobetasol Propionate	27	24
253	Diclofenac	10	15
255	Diflunisal	25	27
266	Fenoprofen	10	ND
294	Losartan	14	14
297	Mefenamic acid	ND	13
325	Progesterone	29	29
338	Spironolactone	24	19
343	Telmisartan	3	7
433	Bromfenac	2	2
473	Cisplatin	68	65
546	Etodolac	5	8
576	Hexachlorophene	42	40
586	Iloperidone	33	27
588	Irbesartan	26	29
620	Meclofenamate	84	86
647	Micafungin	27	28
687	Pazopanib·HCl	37	ND
739	Silver sulfadiazine	70	70
792	Valsartan	4	12
800	Ziprasidone	40	35

IC_{50} values for selected compounds

Entry	Compound	IC_{50} (µM)
82	Olanzapine	20
127	Clozapine	15
136	Indomethacin	>120 (0%)
253	Diclofenac	>363 (5%)
473	Cisplatin	27
620	Meclofenamate	14
739	Silver sulfadiazine	<1
--	Aceclofenac	>429 (20%)
--	BIM1	>123 (0%)
--	BIM4	>96 (7%)
DPC	*N*-phenylanthranilic acid	>312 (27%)
--	Lubiprostone	>120 (5%)
NFA	Niflumic acid	>120 (0%)
--	Salsalate	>120 (1%)
--	Sodium sulfadiazine	>169 (3%)

EXDENDED DATA FIGURE 2

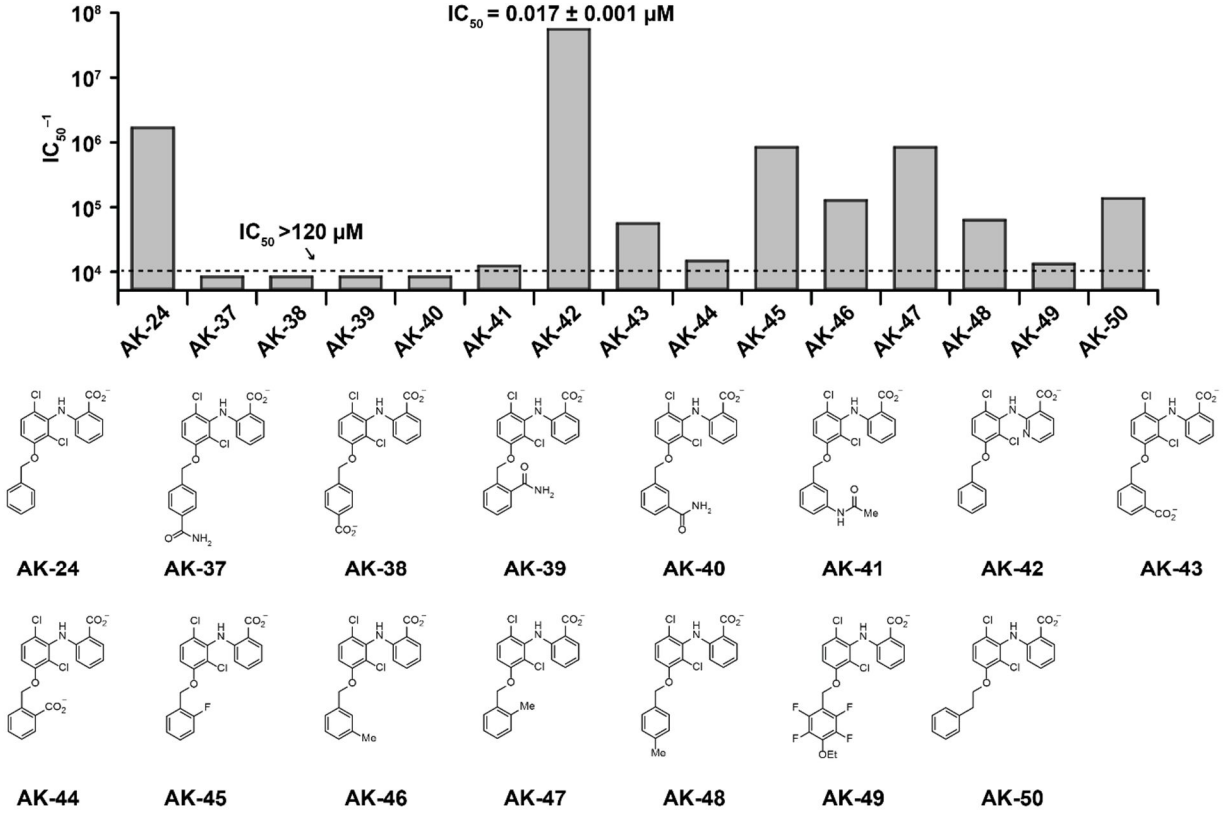

Extended Data Figure 2. SAR studies around the AK-24 scaffold. The bar graphs shows the inverse IC_{50}, estimated from inhibition at four concentrations (n = 3–4 each concentration), as in **Figure 1**. Substitutions around the –OBn ring are destabilizing. Combining the substitutions of AK-24 and AK-33 has a synergistic effect on inhibitor potency (AK-42). Data are tabulated in **Extended Data Table 2**.

EXTENDED DATA TABLE 2

Top Table: Approximate IC_{50} values of fenamate derivatives against CLC-2, determined from 4 concentrations with the IWB platform. Compounds are listed according to position of modification as shown in **Figure 1B** and groups are colored accordingly. *Bottom Table:* IC_{50} data summary for derivatives of AK-24, determined from 4 concentrations with the IWB platform. For both tables, if the IC_{50} was greater than the highest concentration tested, this concentration is listed along with the % inhibition at this concentration (in parenthesis).

Compound	IC_{50} (µM)	Compound	IC_{50} (µM)
Western Ring Deletions		**2,6-Substitutions**	
AK-3	>120 (43%)	**AK-4**	22
AK-4	22	**AK-8**	>120 (41%)
AK-6	>120 (48%)	**AK-15**	23
DPC	>312 (27%)	**AK-21**	86
Chloro- Substitutions		**Nicotinic Acids**	
AK-1	>120 (13%)	**AK-30**	>222 (12%)
AK-2	>120 (12%)	**AK-31**	>42 (16%)
AK-4	22	**AK-32**	115
AK-5	>120 (23%)	**AK-33**	2
AK-7	>120 (22%)	**Eastern Ring**	
C3-Substitutions		**AK-10**	25
AK-13	10	**AK-11**	38
AK-14	7	**AK-12**	>102 (37%)
AK-16	8	**AK-22**	14
AK-17	36	**Anion Substitutions**	
AK-23	2	**AK-9**	>120 (28%)
AK-24	0.6	**AK-18**	33
AK-25	13	**AK-19**	>141 (36%)
AK-26	3	**AK-20**	>144 (8%)
AK-27	5	**AK-34**	>195 (6%)
AK-28	4	**AK-35**	>354 (41%)
AK-29	49	**AK-36**	42
AK-51	>120 (7%)	**DF**	>363 (5%)
MCFA	14		

Compound	IC_{50} (µM)	Compound	IC_{50} (µM)
AK-24	0.6	**AK-44**	68
AK-37	>120 (15%)	**AK-45**	1
AK-38	>120 (4%)	**AK-46**	8
AK-39	>120 (0%)	**AK-47**	1
AK-40	>120 (5%)	**AK-48**	16
AK-41	82	**AK-49**	76
AK-42	<0.12 (90%)	**AK-50**	7
AK-43	18		

FIGURE 2

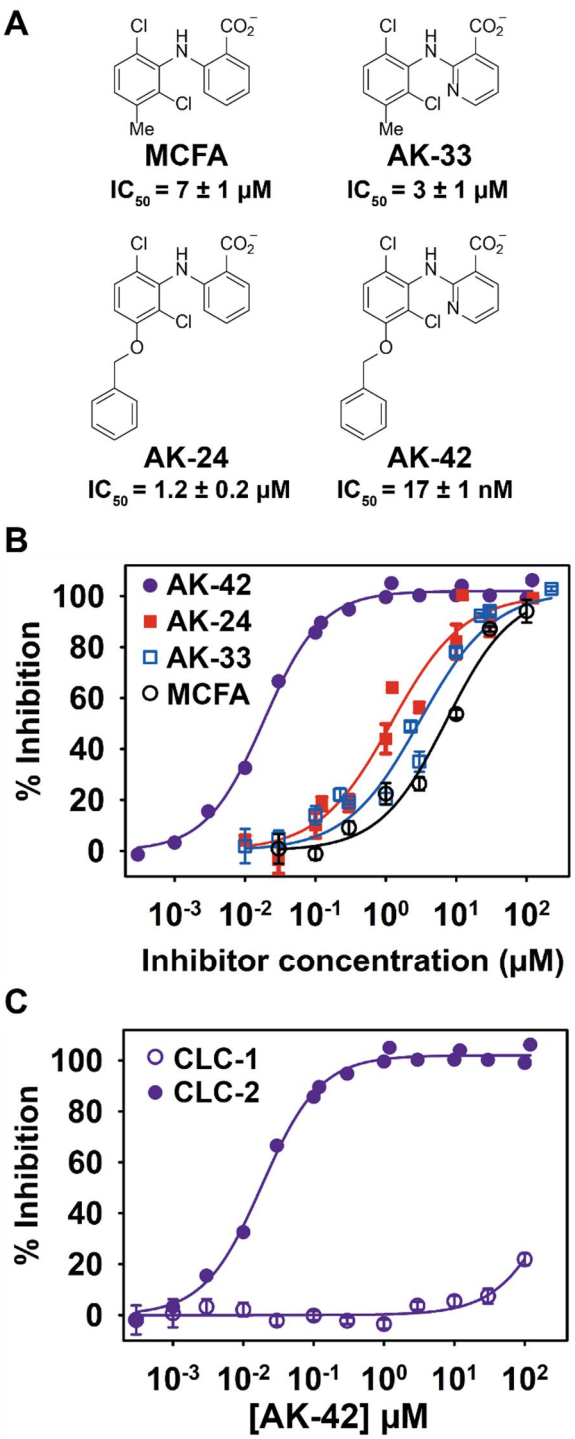

Figure 2. Combining the most potent compounds identified in the SAR studies generates a highly potent and selective CLC-2 inhibitor, AK-42. (**A**) Structures, including the initial 'hit' compound MCFA, are shown. IC_{50} values were determined from data in panel (**B**); these differ slightly from IC_{50} values obtained in the initial screen (**Fig. 1**), which used only four concentrations of each compound. (**B**) Inhibition at –120 mV was determined using the IWB, n = 3–4 for each concentration ± SEM. Fits to the Hill equation yield IC_{50} values of 7 ± 1 μM, 1.2 ± 0.2 μM, 3 ± 1 μM, and 0.017 ± 0.001 μM for MCFA, AK-24, AK-33, and AK-42 respectively (**Extended Data Table 3**). (**C**) Inhibition curves for AK-42 against CLC-1 and CLC-2 determined using the IWB, illustrating that AK-42 is ~10,000 times more potent against CLC-2 compared to the most closely related CLC homolog (individual data points are shown in **Extended Data Table 4**).

EXTENDED DATA FIGURE 3

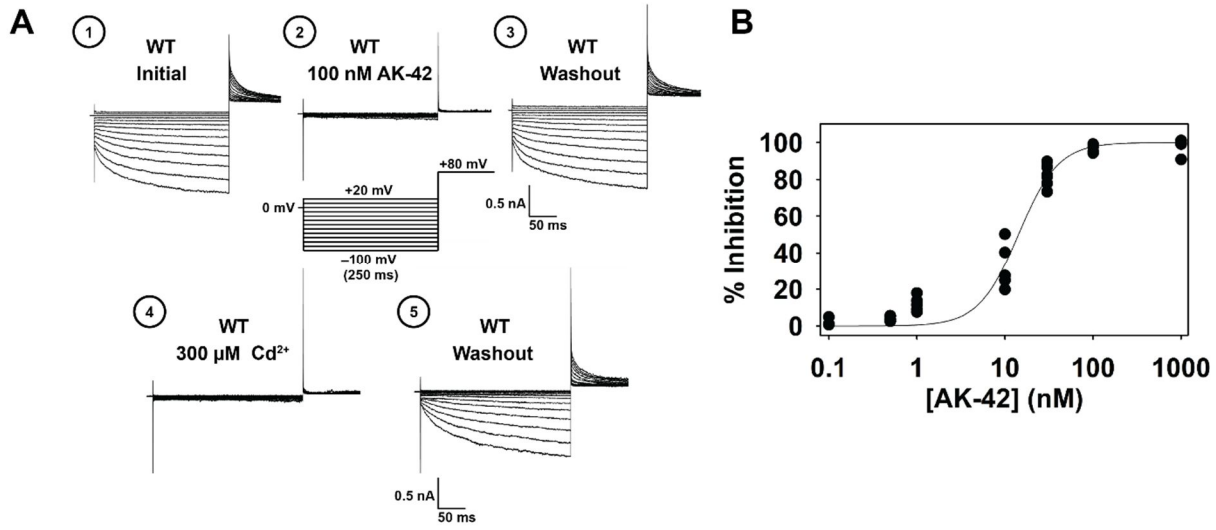

Extended Data Figure 3. Manual patch-clamp recording of rat CLC-2. (**A**) Representative traces showing rat CLC-2 currents in transiently transfected CHO cells in response to the voltage protocol shown: before, after, and following washout of 100 nM AK-42. A saturating concentration of Cd^{2+} (the low-potency CLC-2 inhibitor used in assay development, **Extended Data Fig. 1**) was added at the end of each experiment (Step 4) to facilitate subtraction of background currents on a given cell, and the Cd^{2+} was subsequently washed out (Step 5). Steps 1–5 of a typical experiment are shown. (**B**) Summary inhibition data for AK-42 concentration. Individual data points are shown for inhibition at –100 mV for 0.1 nM (n = 3), 0.5 nM (n = 3), 1 nM (n = 5), 10 nM (n = 5), 30 nM (n = 6), 100 nM (n = 4), 1 µM (n = 4). The fitted IC_{50} value (14 ± 1 nM) is comparable to that obtained for human CLC-2 in the IWB assay (17 ± 1 nM at –120 mV).

EXTENDED DATA TABLE 3

Final IC_{50} values for selected compounds against human CLC-1 and human CLC-2, using the IWB platform. If the IC_{50} was greater than the highest concentration tested, this concentration is listed along with the % inhibition at this concentration (in parenthesis). *For MCFA, the maximum inhibition of CLC-1 at 100 µM was 61%; thus, this IC_{50} value is an approximation.

Compound	IC_{50} (CLC-2)	IC_{50} (CLC-1)
MCFA	7 ± 1 µM	~50 µM*
AK-24	1.2 ± 0.2 µM	>30 µM (25%)
AK-33	3 ± 1 µM	>30 µM (5%)
AK-42	0.017 ± 0.001 µM	>100 µM (22%)

EXTENDED DATA TABLE 4

% inhibition values for human CLC-1 and human CLC-2 with AK-42, as shown in **Figure 2**. Values of over 100% reflect that some current measurements at –120 mV flipped from negative to slightly positive in the presence of inhibitor.

Concentration (µM)	% inhibition, CLC-1	% inhibition, CLC-2
0.0003	–2 ± 6 % (n = 4)	–1 ± 6 % (n = 4)
0.001	1 ± 6 % (n = 4)	3 ± 3 % (n = 4)
0.003	3 ± 3 % (n = 4)	15 ± 4 % (n = 4)
0.01	2 ± 3 % (n = 4)	32 ± 4 % (n = 4)
0.03	–2 ± 2 % (n = 8)	67 ± 2 % (n = 8)
0.1	0 ± 2 % (n = 7)	86 ± 1 % (n = 8)
0.12	not determined (nd)	90 ± 5 % (n = 4)
0.3	–2 ± 1 % (n = 7)	95 ± 2 % (n = 8)
1	–4 ± 2 % (n = 7)	100.0 ± 0.3 % (n = 8)
1.2	nd	105.1 ± 0.7 % (n = 4)
3	4 ± 2 % (n = 4)	100.3 ± 0.4 % (n = 4)
10	5 ± 2 % (n = 4)	100.3 ± 0.4 % (n = 4)
12	nd	104.0 ± 0.8 % (n = 3)
30	7 ± 3 % (n = 4)	100.3 ± 0.3 % (n = 4)
100	22 ± 2 % (n = 4)	99.1 ± 0.2 % (n = 4)
120	nd	106.3 ± 0.5 % (n = 4)

EXTENDED DATA FIGURE 4

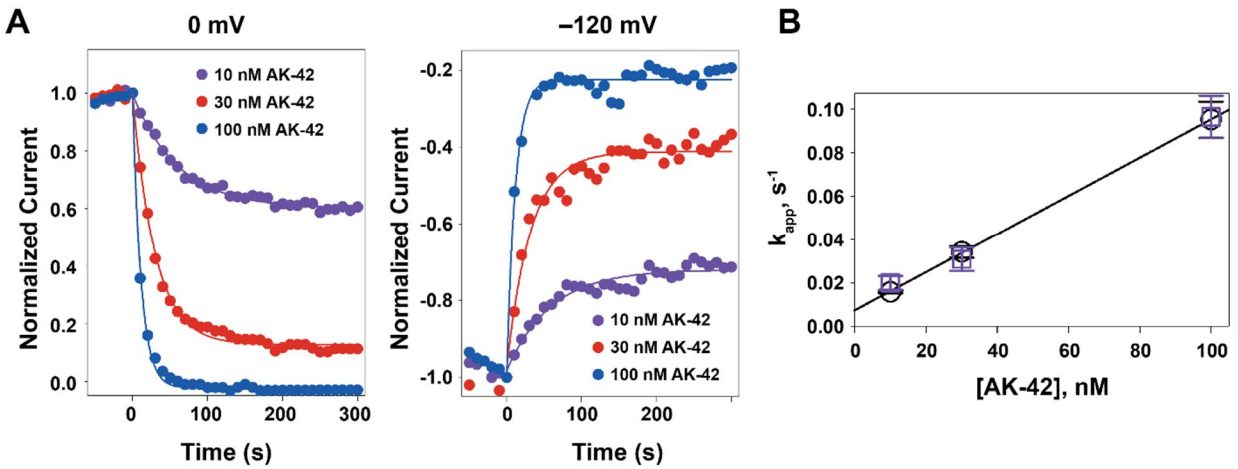

Kinetics CLC-2 inhibition support that AK-42 acts at a single site from the extracellular side. (**A**) Representative data showing the time course of CLC-2 inhibition by 10, 30, or 100 nM of AK-42. Currents were measured using the IWB; cells were held at the reversal potential (–30 mV), and currents were measured with 2-s test pulses to –120 mV followed by 0.5-s tail pulses to 0 mV, every 10 s. The peak current amplitudes in both the test and tail pulses were measured and plotted as a function of time. Data were fitted with a single exponential function to obtain values for k_{app} (apparent rate constant). (**B**) Plot of k_{app} values as a function of AK-42 concentration at -120 mV (purple) or 0 mV (black) for n = 3 (10 nM) or n = 4 (30 nM, 100 nM) cells. The linear relationship between k_{app} and AK-42 illustrates that inhibition is a first-order process, involving a 1:1 CLC-2 subunit/AK-42 interaction. Regression analysis (fitting simultaneously to both sets of points) yields estimates for on- and off-rates of 9×10^5 $M^{-1}s^{-1}$ (slope) and 8×10^{-3} s^{-1} (intercept). While the IWB is not set up to allow measurements of reversal, we confirmed reversibility of inhibition using manual patch-clamp (**Extended Data Figure 3**), with reversal occurring within ~10 min, consistent with the off-rate estimated using the IWB.

FIGURE 3

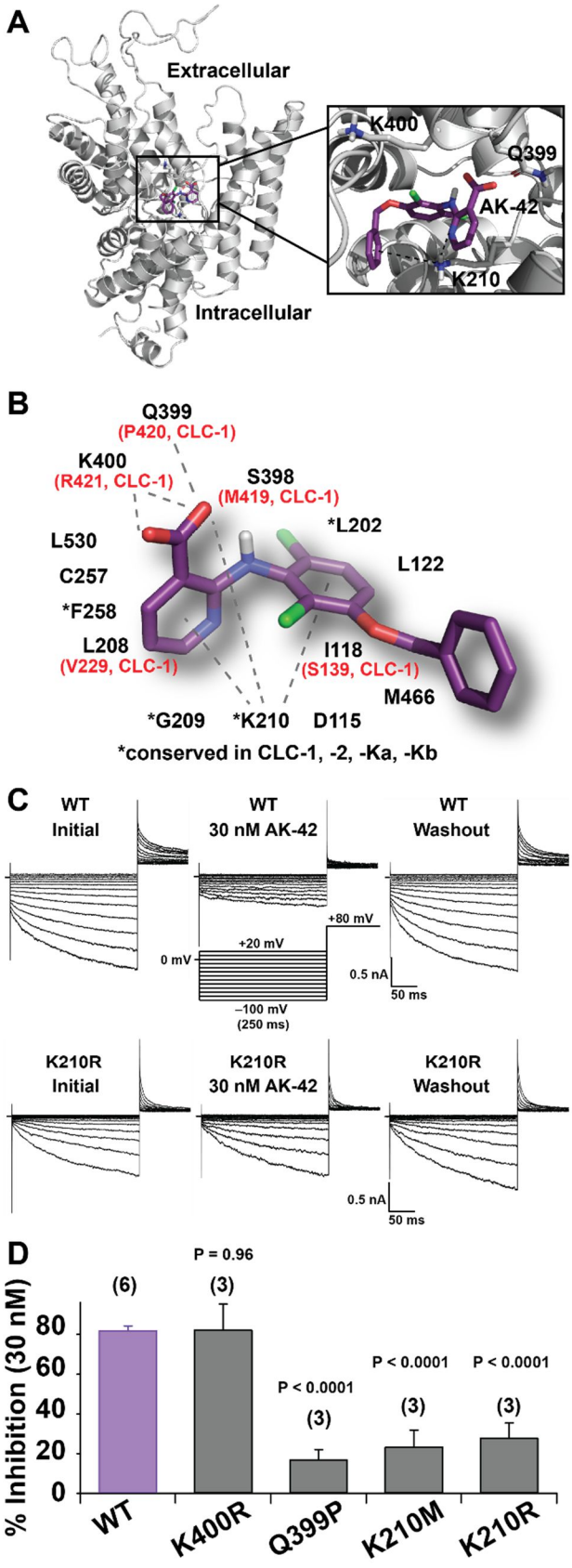

Figure 3. Analysis of AK-42 selectivity and the inhibitory binding site. (**A**) One subunit of the CLC-2 homodimer is shown. AK-42 docks near the extracellular entrance to the chloride permeation pathway, which is tilted towards the viewer. The expanded view highlights 3 of the residues in the predicted binding pocket. (**B**) Illustration of one of the top poses adopted by AK-42 in molecular docking to CLC-2, together with a schematic of the 14 residues observed near AK-42 in all docking poses. Residues differing between CLC-1 and CLC-2 are indicated in red text. (**C**) Representative CLC-2 current traces from manual patch-clamp experiments. *Top:* WT CLC-2 currents, illustrating reversible CLC-2 inhibition by 30 nM of AK-42, consistent with an extracellular binding site. *Bottom:* K210R CLC-2 currents, illustrating a diminution in AK-42 potency upon mutating K to R, supporting the docking model in **B**. (**D**) Testing other residues predicted to interact with AK-42 in the CLC-2 binding site. Mutations of K210 and Q399 produced statistically significant (by unpaired t-test) effects on inhibitor binding at 30 nM, while the mutation K400R did not. Number of data points per mutant is shown in parenthesis. Summary data are tabulated in **Extended Data Table 5**. These data support that AK-42 binds in the pocket predicted by our docking studies.

EXTENDED DATA TABLE 5

% inhibition values for WT CLC-2 and four mutants (K400R, Q399P, K210M, K210R) with 30 nM AK-42 at –100 mV, as shown in **Figure 3D**.

CLC-2 plasmid	% inhibition
WT	82 ± 3 % (n = 6)
K400R	82 ± 13 % (n = 3)
Q399P	17 ± 5 % (n = 3)
K210M	23 ± 9 % (n = 3)
K210R	27 ± 8 % (n = 3)

FIGURE 4

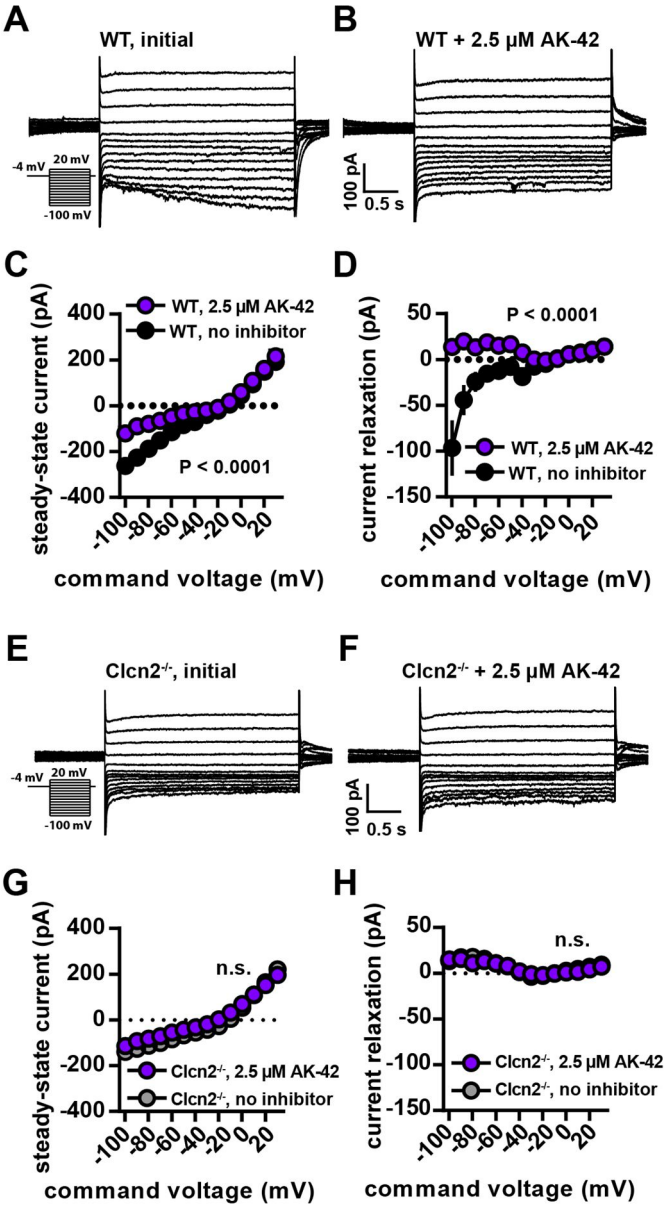

Figure 4. AK-42 inhibits hyperpolarization-activated current in hippocampal cells. (**A–B**) Whole-cell voltage-clamp recordings (protocol in inset) of WT mouse CA1 pyramidal neurons with and without AK-42. Capacitive transients are clipped for display purposes. (**C**) Whole-cell I-V relationship at steady-state both with and without AK-42 (n = 5 cells, 6 slices and 2 animals per group. P < 0.0001 via two-way RM ANOVA). Error bars represent ± SEM throughout. (**D**) Current relaxation measured as the difference between the beginning and end of a 4-s pulse, showing that development of inward current was blocked by AK-42 (n = 6 cells, 6 slices and 2 animals per group. P < 0.0001 via two-way RM ANOVA). (**E–F**) Whole-cell currents from voltage-clamp recordings of *Clcn2*$^{-/-}$ CA1 pyramidal neurons before and after AK-42 treatment. Unlike WT responses, steady-state responses show no differences after AK-42 treatment at negative membrane potentials. Steady-state currents (**G**) and current relaxation (**H**) in *Clcn2*$^{-/-}$ cells show no difference after AK-42 treatment (n = 6 cells, 6 slices and 2 animals per group. P = 0.25 and 0.97 for steady-state and current relaxation measurements, respectively, via two-way RM ANOVA.

EXTENDED DATA FIGURE 5

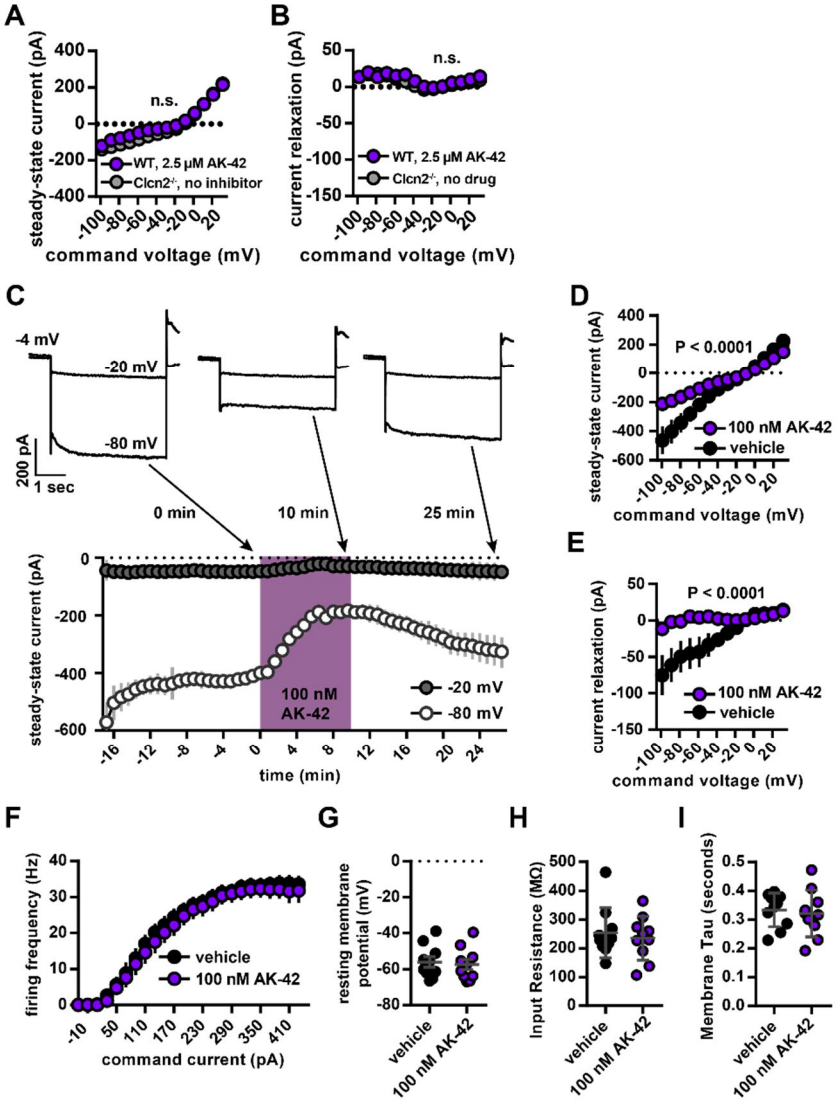

Extended Data Figure 5. Confirmation of AK-42 efficacy and specificity.
(**A–B**): *Clcn2*$^{-/-}$ control. Steady-state currents (**A**) and current relaxation measurements (**B**) are indistinguishable between wild-type cells treated with 2.5 μM AK-42 and untreated *Clcn2*$^{-/-}$ (P = 0.53 and 0.63 for **A** and **B**, respectively via two-way RM ANOVA.)
(**C–E**): AK-42 is effective and reversible at 100 nM. (**C**) Time course (bottom) and representative whole-cell current traces (top) show reversible inhibition of CLC-2 by 100 nM AK-42. Note that AK-42 visibly decreases current at hyperpolarized (–80 mV) but not depolarized (–20 mV) potentials. Capacitive transients are clipped for display purposes. (**D–E**) Summary data showing I-V relationship of WT whole-cell steady-state currents (**D**) and current relaxation (**E**) before and after 10 minutes of AK-42 treatment at 100 nM (n = 6 cells, 6 slices and 6 animals. P < 0.0001 via two-way RM ANOVA).
(**F–I**): Specificity of AK-42 as evidenced by lack of effects on firing frequency and membrane parameters. (**F**) Firing frequency of CA1 pyramidal cells in response to a 500-ms current injection is not changed after the application of 100 nM AK-42 for 10 minutes. Error bars represent ± SEM throughout. (P = 0.66 via two-way RM ANOVA. N = 10 cells, 10 slices from 6 animals). (**G–I**) Membrane parameters remain unchanged after 10 minutes of AK-42 application (100 nM), calculated from current-clamp recordings in panel F. (P = 0.73, 0.61, and 0.71, respectively, via Student's unpaired *T*-test.)

FIGURE 5

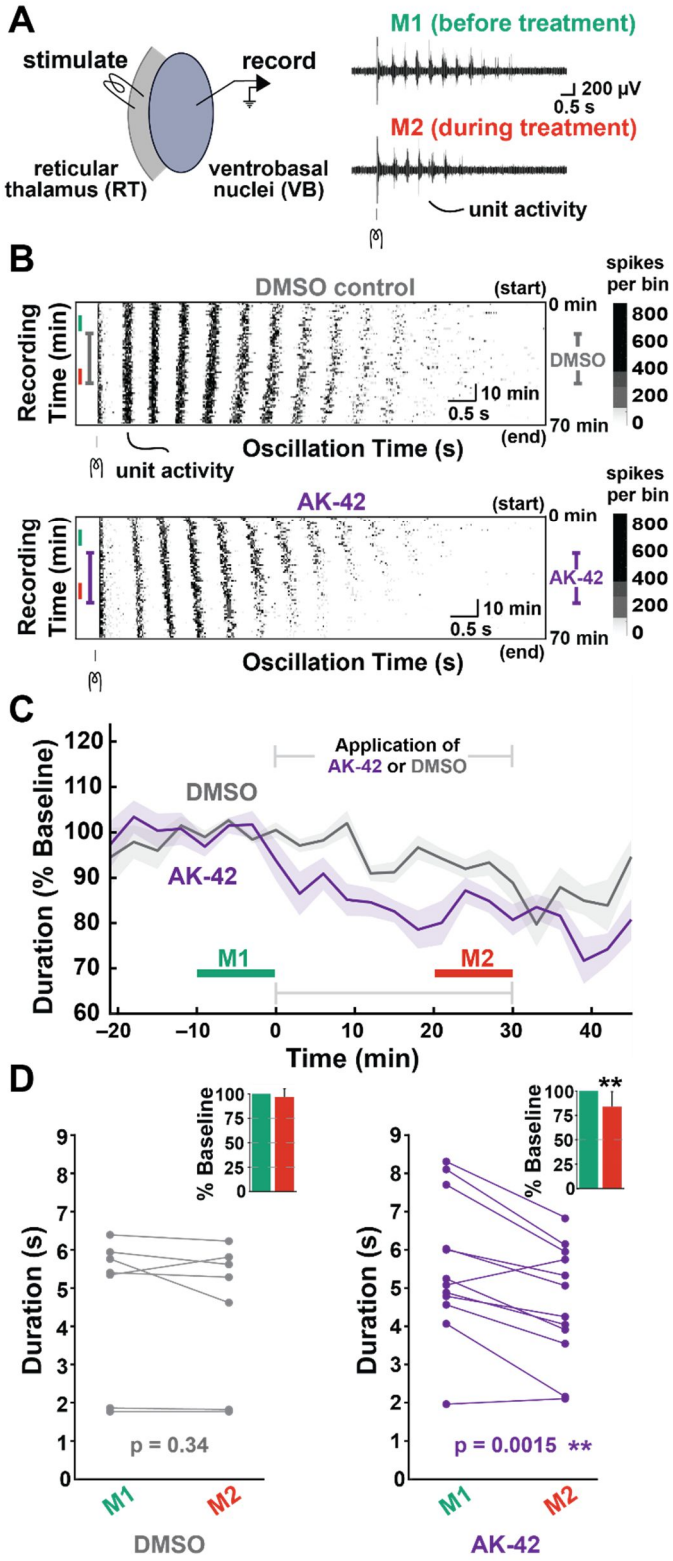

Figure 5. AK-42 dampens epileptiform network oscillations in the acute thalamic brain slice. (**A**) *Left:* Acute brain slices containing the reticular thalamus (RT) and ventrobasal (VB) nuclei were electrically stimulated with a bipolar electrode placed within RT and monitored with an extracellular recording electrode placed within VB. A single shock reliably evoked seconds-long rhythmic activity. *Right:* Representative oscillations recorded at the beginning of the experiment (measurement 1 = M1, top, green) were shortened when 100 nM AK-42 was applied (measurement 2 = M2, bottom, red). (**B**) Time course of oscillations for a single experiment before, during, and after application of a vehicle control (DMSO, gray, top panel) or AK-42 (purple, bottom panel). The experimenter was blinded to condition (i.e. AK-42 vs. control). Evoked action potentials are presented in raster format, and each horizontal line represents a single, evoked oscillation within the experiment. (**C, D**) Summary data showing that AK-42 shortens the duration of evoked oscillations. In **C**, the duration of each evoked oscillation within an experiment was normalized to the mean oscillation duration immediately prior to switching to AK-42 or vehicle control application. Normalized oscillation durations were binned in 3-minute epochs (dark line indicates the mean; shaded area indicates the standard error). Panel **D** shows paired results from independent experiments, highlighting that oscillation duration was unchanged following DMSO application (left, n = 7), but shorter following AK-42 plus DMSO application (right, n = 12). M1 (baseline) values (green) correspond to the mean duration of evoked oscillations in the 10 minutes prior to DMSO or DMSO/AK-42 application. M2 values (red) correspond to the mean duration of evoked oscillations following DMSO or DMSO/AK-42 application, in the 10 minutes prior to washout. Insets show baseline-normalized values.

References

1 Hodgkin, A. L. & Huxley, A. F. The components of membrane conductance in the giant axon of Loligo. *J. Physiol.* **116**, 473-496 (1952).

2 Walz, W. Chloride/anion channels in glial cell membranes. *Glia* **40**, 1-10 (2002).

3 Wilson, C. S. & Mongin, A. A. The signaling role for chloride in the bidirectional communication between neurons and astrocytes. *Neurosci. Lett.* **689**, 33-44, doi:10.1016/j.neulet.2018.01.012 (2019).

4 Stauber, T. & Jentsch, T. J. Chloride in vesicular trafficking and function. *Annu. Rev. Physiol.* **75**, 453-477, doi:10.1146/annurev-physiol-030212-183702 (2013).

5 Rahmati, N., Hoebeek, F. E., Peter, S. & De Zeeuw, C. I. Chloride Homeostasis in Neurons With Special Emphasis on the Olivocerebellar System: Differential Roles for Transporters and Channels. *Frontiers in cellular neuroscience* **12**, 101, doi:10.3389/fncel.2018.00101 (2018).

6 Watanabe, M. & Fukuda, A. Development and regulation of chloride homeostasis in the central nervous system. *Frontiers in cellular neuroscience* **9**, 371, doi:10.3389/fncel.2015.00371 (2015).

7 Olsen, R. W. in *Neuropsychopharmacology - 5th Generation of Progress* (eds K.L. Davis, D. Charney, J.T. Coyle, & C. Nemeroff) Ch. 12, 159-168 (Lippincott, Williams, & Wilkins, 2002).

8 Olsen, R. W. & Sieghart, W. GABA A receptors: subtypes provide diversity of function and pharmacology. *Neuropharmacology* **56**, 141-148, doi:10.1016/j.neuropharm.2008.07.045 (2009).

9 Jentsch, T. J. & Pusch, M. CLC Chloride Channels and Transporters: Structure, Function, Physiology, and Disease. *Physiol. Rev.* **98**, 1493-1590, doi:10.1152/physrev.00047.2017 (2018).

10 Thiemann, A., Grunder, S., Pusch, M. & Jentsch, T. J. A chloride channel widely expressed in epithelial and non-epithelial cells. *Nature* **356**, 57-60 (1992).

11 Blanz, J. *et al.* Leukoencephalopathy upon disruption of the chloride channel ClC-2. *J. Neurosci.* **27**, 6581-6589 (2007).

12 Bosl, M. R. *et al.* Male germ cells and photoreceptors, both dependent on close cell-cell interactions, degenerate upon ClC-2 Cl(-) channel disruption. *EMBO J.* **20**, 1289-1299 (2001).

13 Nehrke, K. *et al.* Loss of hyperpolarization-activated Cl(-) current in salivary acinar cells from Clcn2 knockout mice. *The Journal of Biological Chemistry* **277**, 23604-23611 (2002).

14 Haug, K. *et al.* Mutations in CLCN2 encoding a voltage-gated chloride channel are associated with idiopathic generalized epilepsies. *Nat. Genet.* **33**, 527-532 (2003).

15 D'Agostino, D. *et al.* Mutations and polymorphisms of the CLCN2 gene in idiopathic epilepsy. *Neurology* **63**, 1500-1502 (2004).

16 Saint-Martin, C. *et al.* Two novel CLCN2 mutations accelerating chloride channel deactivation are associated with idiopathic generalized epilepsy. *Hum. Mutat.* **30**, 397-405 (2009).

17 Kleefuss-Lie, A. *et al.* CLCN2 variants in idiopathic generalized epilepsy. *Nat. Genet.* **41**, 954-955 (2009).

18 Everett, K. *et al.* Linkage and mutational analysis of CLCN2 in childhood absence epilepsy. *Epilepsy Res.* **75**, 145-153 (2007).

19 Stogmann, E. *et al.* Mutations in the CLCN2 gene are a rare cause of idiopathic generalized epilepsy syndromes. *Neurogenetics* **7**, 265-268, doi:10.1007/s10048-006-0057-x (2006).

20 Bertelli, M. *et al.* Quantification of chloride channel 2 (CLCN2) gene isoforms in normal versus lesion- and epilepsy-associated brain tissue. *Biochim. Biophys. Acta* **1772**, 15-20, doi:10.1016/j.bbadis.2006.10.015 (2007).

21 Combi, R. *et al.* Clinical and genetic familial study of a large cohort of Italian children with idiopathic epilepsy. *Brain Res. Bull.* **79**, 89-96, doi:10.1016/j.brainresbull.2009.01.008 (2009).

22 Haug, K. *et al.* Retraction: Mutations in CLCN2 encoding a voltage-gated chloride channel are associated with idiopathic generalized epilepsies. *Nat. Genet.* **41**, 1043, doi:10.1038/ng0909-1043 (2009).

23 Niemeyer, M. I. *et al.* No evidence for a role of CLCN2 variants in idiopathic generalized epilepsy. *Nat. Genet.* **42**, 3, doi:10.1038/ng0110-3 (2010).

24 Clark, S., Jordt, S. E., Jentsch, T. J. & Mathie, A. Characterization of the hyperpolarization-activated chloride current in dissociated rat sympathetic neurons. *J. Physiol.* **506**, 665-678 (1998).
25 Nobile, M., Pusch, M., Rapisarda, C. & Ferroni, S. Single-channel analysis of a ClC-2-like chloride conductance in cultured rat cortical astrocytes. *FEBS. Lett.* **479**, 10-14 (2000).
26 Staley, K. The role of an inwardly rectifying chloride conductance in postsynaptic inhibition. *J. Neurophysiol.* **72**, 273-284 (1994).
27 Smith, R. L., Clayton, G. H., Wilcox, C. L., Escudero, K. W. & Staley, K. J. Differential expression of an inwardly rectifying chloride conductance in rat brain neurons: a potential mechanism for cell-specific modulation of postsynaptic inhibition. *J. Neurosci.* **15**, 4057-4067 (1995).
28 Sik, A., Smith, R. L. & Freund, T. F. Distribution of chloride channel-2-immunoreactive neuronal and astrocytic processes in the hippocampus. *Neuroscience.* **101**, 51-65 (2000).
29 Sigma-Aldrich. *The Handbook of Receptor Classification and Signal Transduction*. (Merck KGaA, 2019).
30 Suh, K. S. & Yuspa, S. H. Intracellular chloride channels: critical mediators of cell viability and potential targets for cancer therapy. *Curr. Pharm. Des.* **11**, 2753-2764 (2005).
31 Pusch, M. *et al.* Mechanisms of block of muscle type CLC chloride channels (Review). *Mol. Membr. Biol.* **19**, 285-292 (2002).
32 Cabantchik, Z. I. & Greger, R. Chemical probes for anion transporters of mammalian cell membranes. *Am. J. Physiol.* **262**, C803-827 (1992).
33 Liantonio, A. *et al.* Molecular switch for CLC-K Cl- channel block/activation: optimal pharmacophoric requirements towards high-affinity ligands. *Proc. Natl. Acad. Sci. U. S. A.* **105**, 1369-1373, doi:10.1073/pnas.0708977105 (2008).
34 Gradogna, A. & Pusch, M. Molecular Pharmacology of Kidney and Inner Ear CLC-K Chloride Channels. *Front Pharmacol* **1**, 130, doi:10.3389/fphar.2010.00130 (2010).
35 Liantonio, A. *et al.* Kidney CLC-K chloride channels inhibitors: structure-based studies and efficacy in hypertension and associated CLC-K polymorphisms. *J. Hypertens.* **34**, 981-992, doi:10.1097/HJH.0000000000000876 (2016).
36 Koster, A. K. *et al.* A selective class of inhibitors for the CLC-Ka chloride ion channel. *Proc. Natl. Acad. Sci. U. S. A.* **115**, E4900-E4909, doi:10.1073/pnas.1720584115 (2018).
37 Furukawa, T., Ogura, T., Katayama, Y. & Hiraoka, M. Characteristics of rabbit ClC-2 current expressed in Xenopus oocytes and its contribution to volume regulation. *Am. J. Physiol.* **274**, C500-C512 (1998).
38 Jordt, S. E. & Jentsch, T. J. Molecular dissection of gating in the ClC-2 chloride channel. *EMBO J.* **16**, 1582-1592 (1997).
39 Zuniga, L. *et al.* The voltage-dependent ClC-2 chloride channel has a dual gating mechanism. *J. Physiol.* **555**, 671-682 (2004).
40 Thompson, C. H., Freeman, C.S., French, R.J., McCarty, N.A. Pharmacological Charcterization of GaTx2, a Peptide Inhibitor of ClC-2 Chloride Channels. *Biophys. J.* **96**, 470a (2009).
41 Cuppoletti, J. *et al.* SPI-0211 activates T84 cell chloride transport and recombinant human ClC-2 chloride currents. *Am. J. Physiol. Cell Physiol.* **287**, C1173-1183 (2004).
42 Norimatsu, Y., Moran, A. R. & MacDonald, K. D. Lubiprostone activates CFTR, but not ClC-2, via the prostaglandin receptor (EP(4)). *Biochem. Biophys. Res. Commun.* **426**, 374-379, doi:10.1016/j.bbrc.2012.08.097 (2012).
43 Besnard, J. *et al.* Automated design of ligands to polypharmacological profiles. *Nature* **492**, 215-220, doi:10.1038/nature11691 (2012).
44 McKiernan, K. A., Koster, A. K., Maduke, M. & Pande, V. S. Dynamical model of the CLC-2 ion channel reveals conformational changes associated with selectivity-filter gating. *BioRxiv* **https://www.biorxiv.org/content/10.1101/228163v5** (2019).
45 Park, E., Campbell, E. B. & MacKinnon, R. Structure of a CLC chloride ion channel by cryo-electron microscopy. *Nature* **541**, 500-505, doi:10.1038/nature20812 (2017).

46 Madison, D. V., Malenka, R. C. & Nicoll, R. A. Phorbol esters block a voltage-sensitive chloride current in hippocampal pyramidal cells. *Nature* **321**, 695-697 (1986).
47 Mager, R., Ferroni, S. & Schubert, P. Adenosine modulates a voltage-dependent chloride conductance in cultured hippocampal neurons. *Brain Res.* **532**, 58-62, doi:10.1016/0006-8993(90)91741-x (1990).
48 Foldy, C., Lee, S. H., Morgan, R. J. & Soltesz, I. Regulation of fast-spiking basket cell synapses by the chloride channel ClC-2. *Nat. Neurosci.* **13**, 1047-1049, doi:10.1038/nn.2609 (2010).
49 Lein, E. S. *et al.* Genome-wide atlas of gene expression in the adult mouse brain. *Nature* **445**, 168-176, doi:10.1038/nature05453 (2007).
50 Fogerson, P. M. & Huguenard, J. R. Tapping the Brakes: Cellular and Synaptic Mechanisms that Regulate Thalamic Oscillations. *Neuron* **92**, 687-704, doi:10.1016/j.neuron.2016.10.024 (2016).
51 McCormick, D. A. & Contreras, D. On the cellular and network bases of epileptic seizures. *Annu. Rev. Physiol.* **63**, 815-846, doi:10.1146/annurev.physiol.63.1.815 (2001).
52 Beenhakker, M. P. & Huguenard, J. R. Neurons that fire together also conspire together: is normal sleep circuitry hijacked to generate epilepsy? *Neuron* **62**, 612-632, doi:10.1016/j.neuron.2009.05.015 (2009).
53 Kim, U., Sanchez-Vives, M. V. & McCormick, D. A. Functional dynamics of GABAergic inhibition in the thalamus. *Science* **278**, 130-134, doi:10.1126/science.278.5335.130 (1997).
54 Bal, T. & McCormick, D. A. What stops synchronized thalamocortical oscillations? *Neuron* **17**, 297-308 (1996).
55 Kleiman-Weiner, M., Beenhakker, M. P., Segal, W. A. & Huguenard, J. R. Synergistic roles of GABAA receptors and SK channels in regulating thalamocortical oscillations. *J. Neurophysiol.* **102**, 203-213, doi:10.1152/jn.91158.2008 (2009).
56 von Krosigk, M., Bal, T. & McCormick, D. A. Cellular mechanisms of a synchronized oscillation in the thalamus. *Science* **261**, 361-364, doi:10.1126/science.8392750 (1993).
57 Lin, S. H. *et al.* Prolactin-releasing peptide (PrRP) promotes awakening and suppresses absence seizures. *Neuroscience* **114**, 229-238, doi:10.1016/s0306-4522(02)00248-8 (2002).
58 Huguenard, J. R. & Prince, D. A. Intrathalamic rhythmicity studied in vitro: nominal T-current modulation causes robust antioscillatory effects. *J. Neurosci.* **14**, 5485-5502 (1994).
59 Staley, K., Smith, R., Schaack, J., Wilcox, C. & Jentsch, T. J. Alteration of GABAA receptor function following gene transfer of the CLC-2 chloride channel. *Neuron* **17**, 543-551 (1996).
60 Jin, X., Huguenard, J. R. & Prince, D. A. Impaired Cl- extrusion in layer V pyramidal neurons of chronically injured epileptogenic neocortex. *J. Neurophysiol.* **93**, 2117-2126, doi:10.1152/jn.00728.2004 (2005).
61 Klein, P. M. *et al.* Tenuous Inhibitory GABAergic Signaling in the Reticular Thalamus. *J. Neurosci.* **38**, 1232-1248, doi:10.1523/JNEUROSCI.1345-17.2017 (2018).
62 Misgeld, U., Deisz, R. A., Dodt, H. U. & Lux, H. D. The role of chloride transport in postsynaptic inhibition of hippocampal neurons. *Science* **232**, 1413-1415, doi:10.1126/science.2424084 (1986).
63 Ratte, S. & Prescott, S. A. ClC-2 channels regulate neuronal excitability, not intracellular chloride levels. *J. Neurosci.* **31**, 15838-15843, doi:31/44/15838 [pii]10.1523/JNEUROSCI.2748-11.2011 (2011).
64 Koeleman, B. P. C. What do genetic studies tell us about the heritable basis of common epilepsy? Polygenic or complex epilepsy? *Neurosci. Lett.* **667**, 10-16, doi:10.1016/j.neulet.2017.03.042 (2018).
65 Ferraro, T. N. & Buono, R. J. Polygenic epilepsy. *Adv. Neurol.* **97**, 389-398 (2006).
66 Reid, C. A., Berkovic, S. F. & Petrou, S. Mechanisms of human inherited epilepsies. *Prog. Neurobiol.* **87**, 41-57, doi:10.1016/j.pneurobio.2008.09.016 (2009).
67 Staley, K. Molecular mechanisms of epilepsy. *Nat. Neurosci.* **18**, 367-372, doi:10.1038/nn.3947 (2015).
68 Elorza-Vidal, X., Gaitan-Penas, H. & Estevez, R. Chloride Channels in Astrocytes: Structure, Roles in Brain Homeostasis and Implications in Disease. *Int. J. Mol. Sci.* **20**, doi:10.3390/ijms20051034 (2019).
69 Zhang, J. H., Chung, T. D. & Oldenburg, K. R. A Simple Statistical Parameter for Use in Evaluation and Validation of High Throughput Screening Assays. *J. Biomol. Screen.* **4**, 67-73, doi:10.1177/108705719900400206 (1999).

70 Ting, J. T., Daigle, T. L., Chen, Q. & Feng, G. Acute brain slice methods for adult and aging animals: application of targeted patch clamp analysis and optogenetics. *Methods Mol. Biol.* **1183**, 221-242, doi:10.1007/978-1-4939-1096-0_14 (2014).
71 Pettersen, E. F. *et al.* UCSF Chimera--a visualization system for exploratory research and analysis. *J Comput Chem* **25**, 1605-1612, doi:10.1002/jcc.20084 (2004).
72 Case, D. A. *et al.* The Amber biomolecular simulation programs. *J Comput Chem* **26**, 1668-1688, doi:10.1002/jcc.20290 (2005).
73 Allen, W. J. *et al.* DOCK 6: Impact of new features and current docking performance. *J Comput Chem* **36**, 1132-1156, doi:10.1002/jcc.23905 (2015).
74 Harder, E. *et al.* OPLS3: A Force Field Providing Broad Coverage of Drug-like Small Molecules and Proteins. *Journal of chemical theory and computation* **12**, 281-296, doi:10.1021/acs.jctc.5b00864 (2016).
75 Greenwood, J. R., Calkins, D., Sullivan, A. P. & Shelley, J. C. Towards the comprehensive, rapid, and accurate prediction of the favorable tautomeric states of drug-like molecules in aqueous solution. *J. Comput. Aided Mol. Des.* **24**, 591-604, doi:10.1007/s10822-010-9349-1 (2010).
76 Sali, A. & Blundell, T. L. Comparative protein modelling by satisfaction of spatial restraints. *J. Mol. Biol.* **234**, 779-815, doi:S0022-2836(83)71626-8 [pii]10.1006/jmbi.1993.1626 (1993).
77 Park, E. & MacKinnon, R. Structure of the CLC-1 chloride channel from Homo sapiens. *Elife* **7**, doi:10.7554/eLife.36629 (2018).
78 Friesner, R. A. *et al.* Extra precision glide: docking and scoring incorporating a model of hydrophobic enclosure for protein-ligand complexes. *J. Med. Chem.* **49**, 6177-6196, doi:10.1021/jm051256o (2006).
79 Yusef, Y. R. *et al.* Removal of gating in voltage-dependent ClC-2 chloride channel by point mutations affecting the pore and C-terminus CBS-2 domain. *J. Physiol.* **572**, 173-181 (2006).
80 Pusch, M., Jordt, S., Stein, V. & Jentsch, T. J. Chloride dependence of hyperpolarization-activated chloride channel gates. *J. Physiol.* **515**, 341-353 (1999).
81 Verkman, A. S. & Galietta, L. J. Chloride channels as drug targets. *Nat. Rev. Drug Discov.* **8**, 153-171, doi:nrd2780 [pii]10.1038/nrd2780 (2009).